2.15 The Ab Initio Treatment of High-Pressure and High-Temperature Mineral Properties and Behavior

D Alfè, University College London, London, UK

2.15.1 Introduction

The purpose of this chapter is to provide some examples about recent developments in the calculation of the high-pressure and high-temperature properties of materials using ab initio-based techniques, with the description limited to minerals under the relatively benign conditions of the center of the Earth. This chapter is not intended to review comprehensively all high-pressure and high-temperature ab initio calculations on minerals performed to date nor has the presumption to include the most significant ones. The few examples provided will only serve the purpose of showing what current ab initio techniques are capable of predicting.

With the word 'ab initio,' I refer here to those calculations based on the very basic laws of nature, in which no empirical adjustable parameter is used. Only fundamental constants of physics are allowed. Specifically, since we will be interested in the properties of matter, the relevant basic laws of physics are those describing the interactions between nuclei and electrons, that is, those of quantum mechanics. We shall see that approximations to exact quantum mechanics are necessary to provide tools that can be used in practice; however, as long as these approximations do not involve the introduction of empirical parameters, we will still regard those techniques as ab initio.

I start the discussion by recalling the structure of the Earth, which can be broadly described in terms of three main shells. The outermost is the crust, with a thickness of only a few tens of kilometers, mainly formed by silicates. Below the crust, we find the mantle, which is customarily divided in an upper mantle and a lower mantle, separated by a transition zone. The mantle makes up most of the volume of the Earth, extending to a depth of 2891 km, almost halfway toward the center, and like the crust is also mainly formed by silicates and in particular by $Mg(Fe)SiO_3$ with some significant fraction of $Mg(Fe)O$ and SiO_2. Below the mantle, we find the core, which is divided into an outer liquid core extending from 2891 to 5150 km depths and an inner solid core below that, down to the center of the Earth at 6346 km depth. It is widely accepted that the core is mainly formed by iron, possibly with some 5–10% of nickel,

plus a fraction of unknown light impurities, which reduce the density by 2–3% in the solid and 6–7% in the liquid with respect to the density of pure iron under the same pressure–temperature conditions.

Studying the high-pressure and high-temperature properties of the core- and mantle-forming materials is of fundamental importance to the understanding of the formation and evolution of our planet. In particular, knowledge of the thermal structure of the Earth and the thermoelastic properties of Earth-forming minerals will help us interpret and hopefully predict the behavior of the dynamic processes, which happen inside our planet, including the generation of the Earth's magnetic field through the geodynamo, and the convective processes in the mantle, which are ultimately responsible for plate tectonics, earthquakes, and volcanic eruptions.

The development of theoretical methods based on the very basic laws of nature of quantum mechanics (developed almost 90 years ago), coupled with the recent staggering increase of computer power (∼500-fold in the past 10 years), has made it possible to approach the problem from a theoretical–computational point of view. When high-level first-principles methods are used, the results are often comparable in quality with experiments, sometimes even providing information in regions of the pressure–temperature space unaccessible to experiments.

The exact quantum mechanical treatment of a system containing a large number of atoms is a formidable task. The starting point of nearly every quantum mechanical calculation available is the so-called adiabatic approximation, which exploits the large difference of mass between the nuclei and the electrons. Since the electrons are much lighter, they move so much faster that on the timescale of their movement, the nuclei can be considered as fixed. Therefore, one solves only the electronic problem in which the nuclei are fixed and act as an external potential for the electrons. The energy of the electrons, plus the Coulomb repulsion of the nuclei, is therefore a function of the position of the nuclei and can act as a potential energy for the nuclei. This can be mapped in configuration space to create a potential energy surface, which can later be used to study the motion of the nuclei. Alternatively, forces can be calculated as the derivatives of the potential energy with respect to the position of the nuclei, and these can be used to move the atoms around, relax the system, solve Newton's equations of motion and perform molecular dynamics (MD) simulations, or calculate harmonic vibrational properties like phonons. The potential energy can also be differentiated with respect to the simulation cell parameters, which provides information on the stress tensor. The solution of the electronic problem also provides insights into the electronic structure of the system, which can be examined to study physical properties like bonding, charge distributions, magnetic densities, and polarizabilities.

Most first-principles studies of the high-pressure and high-temperature properties of Earth-forming materials are based on the implementation of quantum mechanics known as density functional theory (DFT). This is a technique that was introduced about 50 years ago by Hohenberg and Kohn (HK) (1964) and Kohn and Sham (KS) (1965) in an attempt to simplify the calculation of the ground-state properties of materials (in fact, later shown to be useful also for finite-temperature properties; Mermin, 1965). The basic HK idea was to substitute the cumbersome many-body wave function of a system containing N particles, which is a function of $3N$ variables, with the particle density, which is only a function of three variables. The price to pay for this enormous simplification is a modification of the basic equations of quantum mechanics with the introduction of new terms, one of which, called exchange-correlation (XC) energy, is unfortunately unknown. However, KS proposed a simple form for the XC functional, known as the local density approximation (LDA) (Kohn and Sham, 1965), that would prove later as the insight that has made DFT so successful and so widespread today. More sophisticated XC functionals were developed in the following decades and are still being developed today, making DFT an evolving technique with increasingly higher accuracy. One additional attractive feature of DFT is the favorable scaling of computational effort with the size of the system. Traditional DFT techniques scale as N^3, where N is the number of electrons in the system, but large effort is being put into the so-called $o(N)$ techniques, which for some materials already provide a scaling that is only directly proportional to the size of the system (Bowler et al., 2002; Soler et al., 2002).

A wide range of properties of minerals have been predicted using DFT techniques, like structural and electronic properties, phase diagrams, thermoelastic properties, speed of sound, transport properties, melting, solutions, and partitioning. In this chapter, we will focus only on a very limited number of applications.

The limitations in accuracy due to the current state of the art of DFT are expected to be progressively removed, either through the formulation of new XC functionals or with the developments of alternative techniques. Among these, dynamic mean field theory (Savrasov and Kotliar, 2003) and quantum Monte Carlo (QMC) (Foulkes et al., 2001) are probably the most promising on a timescale of 5–10 years.

After this introduction, the chapter is divided into two main sections. In the first, I will briefly review the main ideas behind first-principles simulations and in particular DFT and the pseudopotential (PP) approximation. I will also mention QMC techniques as promising advances beyond DFT. Section 2.15.3 will deal with the properties of materials, first at zero temperature and then at finite temperature. Techniques for the calculation of free energies will be presented, and this will be done by separating the low-temperature regime, where solids can be described within the quasi-harmonic approximation, from the high-temperature regime, where the technique of thermodynamics integration is introduced to calculate free energies. The calculation of melting curves and the thermodynamics of solutions will be presented as applications of these techniques. The final section includes recent calculations of the electrical and thermal conductivities of iron and iron alloys at the Earth's core conditions.

2.15.2 First-Principles Techniques

I begin this section by recalling the basic equation of quantum mechanics, the Schrödinger equation, which in the time-independent form is

$$\hat{H}\Psi = E\Psi \qquad [1]$$

where $\hat{H}$ is the Hamiltonian of the system, E the total energy, and Ψ the many-body wave function, which is a function of the coordinates of the M nuclei $\{\mathbf{R}_i\}$ and the N electrons $\{\mathbf{r}_i\}$: $\Psi = \Psi(\mathbf{R}_1, \mathbf{R}_2, \ldots, \mathbf{R}_M; \mathbf{r}_1, \mathbf{r}_2, \ldots, \mathbf{r}_N)$. If the system is isolated, in the nonrelativistic approximation, the Hamiltonian is given by

$$\hat{H}(\mathbf{R}_1, \mathbf{R}_2, \ldots, \mathbf{R}_M; \mathbf{r}_1, \mathbf{r}_2, \ldots, \mathbf{r}_N) = -\sum_{i=1}^{M}\frac{\hbar^2}{2M_i}\nabla_{\mathbf{R}_i}^2 - \sum_{i=1}^{N}\frac{\hbar^2}{2m}\nabla_{\mathbf{r}_i}^2 + \frac{1}{2}\sum_{i,j=1;i\neq j}^{M}\frac{Z_iZ_je^2}{4\pi\varepsilon_0|\mathbf{R}_i - \mathbf{R}_j|} + \frac{1}{2}\sum_{i,j=1;i\neq j}^{N}\frac{e^2}{4\pi\varepsilon_0|\mathbf{r}_i - \mathbf{r}_j|} - \sum_{i=1}^{M}\sum_{j=1}^{N}\frac{Z_ie^2}{4\pi\varepsilon_0|\mathbf{R}_i - \mathbf{r}_j|}$$

$$[2]$$

where the first two terms are the kinetic energy operators for the nuclei and the electrons, respectively, with $\hbar$ the Planck's constant h divided by 2π and M_i and m the masses of the nuclei and the electrons, respectively. The third and the fourth terms in the equation represent the Coulomb repulsive energies between the nuclei and between the electrons, respectively, with Z_i the charges of the nuclei in units of e, the charge of the electron, and ε_0 the dielectric constant of the vacuum. The last term of the equation represents the electrostatic interaction between the electrons and the nuclei.

The only experimental input in the Schrödinger equation in the nonrelativistic approximation is the four fundamental constants: the Plank's constant h, the charge of the electron e, the mass of the electron m, and the dielectric constant of the vacuum ε_0, which are the same for every system, plus the mass of the nuclei.

As mentioned in Section 2.15.1, solving the Schrödinger equation is essentially impossible for any real system more complicated than the hydrogen atom or more generally any system, which contains three or more quantum particles, and therefore, approximations are needed to make the problem manageable. The first approximation, which can be brought in, is the Born–Oppenheimer approximation, also called the adiabatic approximation. Here, one recognizes that the masses of the nuclei M_i are much larger than the mass of the electron m (the lightest possible atom is the hydrogen atom, which is almost 2000 times heavier than the electron), which therefore move on a much faster timescale. This means that, without much loss of accuracy for most systems, one can separate the electronic problem from that of the nuclei or in other words solve the Schrödinger equation for the electrons only, with the nuclei positions kept fixed. Therefore, we can rewrite eqn [1] as

$$\hat{H}(\mathbf{r}_1, \mathbf{r}_2, \ldots, \mathbf{r}_M; \{\mathbf{R}_i\})\Psi(\mathbf{r}_1, \mathbf{r}_2, \ldots, \mathbf{r}_M; \{\mathbf{R}_i\})$$
$$= E\{\mathbf{R}_i\}\Psi(\mathbf{r}_1, \mathbf{r}_2, \ldots, \mathbf{r}_M; \{\mathbf{R}_i\}) \qquad [3]$$

where now the Hamiltonian depends only parametrically from the positions of the nuclei $\{\mathbf{R}_i\}$, and so do the wave function Ψ and the energy E. Once eqn [3] is solved, the energy $E\{\mathbf{R}_i\}$ can be interpreted as a potential energy for the motion of nuclei. At high temperature (above the Debye temperature), the quantum nature of the nuclei becomes negligible, and with essentially no loss of accuracy, one can treat their motion as they were classical particles. This allows to perform MD simulations, in which the Newton equations of motion for the nuclei are solved using the quantum mechanical forces evaluated from the derivative of $E\{\mathbf{R}_i\}$ with respect to the positions $\{\mathbf{R}_i\}$. If the quantum nature of the nuclei is important (e.g., hydrogen), this can be described using path integral techniques

(Feynman, 1948; a very clear description of path integral methods can be found in Gillan (1990)).

2.15.2.1 Density Functional Theory

The introduction of DFT in 1964 by Hohenberg and Kohn (1964) tackled the many-body problem using a completely new approach. I will briefly outline here the main ideas of DFT; for an in-depth description of DFT, the reader may consult the original papers or the excellent books by Parr and Wang (1989) or Dreizler and Gross (1990) or the recent book by Martin (2004). A simplified (almost) nonmathematical explanation of DFT has been given by Gillan (1997).

Hohenberg and Kohn (1964) proved that the external potential V_{ext} acting on the electrons is uniquely determined (up to a trivial additive constant) by the electron ground-state density $n(\mathbf{r}) = \langle\Psi|\hat{n}(\mathbf{r})|\Psi\rangle = \int d\mathbf{r}_2, \ldots, d\mathbf{r}_N|\Psi(\mathbf{r}, \mathbf{r}_2, \ldots, \mathbf{r}_N)|^2$, where Ψ is the ground-state wave function of the system and $\hat{n}(\mathbf{r})$ is the density operator. Here, we have omitted the dependence of Ψ from the positions of the nuclei for simplicity. Since $n(\mathbf{r})$ determines also the number of electrons N and since V_{ext} and N fix the Hamiltonian of the system, it turns out that the electron density completely determines all the electronic ground-state properties of the system and in fact, as shown later by Mermin (1965), also the finite-temperature properties.

One important property of the system is the energy, which can be written as

$$E[n] = F_{\text{HK}}[n] + \int V_{\text{ext}}(\mathbf{r})n(\mathbf{r})d\mathbf{r} \qquad [4]$$

with

$$F_{\text{HK}}[n] = \langle\Psi[n]|\hat{T} + \hat{V}_{\text{ee}}|\Psi[n]\rangle \qquad [5]$$

where $\hat{T}$ and $\hat{V}_{\text{ee}}$ are, respectively, the kinetic energy and the electron–electron interaction operators and $\Psi[n]$ is the ground-state wave function of the system. Note that $F_{\text{HK}}[n]$ does not depend on the external potential and therefore it is a universal functional. This is the crucial result of DFT. Using the variational principle, HK also proved that the ground-state density of the system is the one that minimizes $E[n]$ and the minimum of $E[n]$ is equal to the ground-state energy E_0. The importance of these two results is clear; the only quantity that is needed is the electron density, no matter how many electrons are present in the system.

One year after the publication of the HK paper, KS invented an indirect method to solve the problem (Kohn and Sham, 1965). The idea is to write the energy functional as an easy part plus a difficult part:

$$F[n] = T_0[n] + E_{\mathrm{H}}[n] + E_{\mathrm{xc}}[n] \qquad [6]$$

where $T_0[n]$ is the ground-state kinetic energy of an auxiliary noninteracting system whose density is the same as the one of the real system, $E_{\mathrm{H}}[n]$ is the repulsive electrostatic energy of the classical charge distribution $n(\mathbf{r})$, and $E_{\mathrm{xc}}[n]$ is the XC energy defined through eqn [6].

Minimizing the total energy $E[n]$ under the constraints of orthonormality for the one-particle orbitals of the auxiliary system, $\int \psi_i^*(\mathbf{r})\psi_j(\mathbf{r})\mathrm{d}\mathbf{r} = \delta_{ij}$, one finds a set of one-particle Schrodinger-like equations:

$$\left[-\frac{\hbar^2}{2m}\nabla^2 + V_{\mathrm{KS}}(\mathbf{r}) \right] \psi_i(\mathbf{r}) = \varepsilon_i \psi_i(\mathbf{r}) \qquad [7]$$

where the KS potential is

$$V_{\mathrm{KS}}(\mathbf{r}) = V_{\mathrm{ext}}(\mathbf{r}) + \int \frac{n(\mathbf{r}')}{|\mathbf{r}-\mathbf{r}'|}\mathrm{d}\mathbf{r}' + V_{\mathrm{xc}}(\mathbf{r}); \; V_{\mathrm{xc}}(\mathbf{r}) = \frac{\delta E_{\mathrm{xc}}[n]}{\delta n(\mathbf{r})} \qquad [8]$$

and

$$n(\mathbf{r}) = \sum_i f(\varepsilon_i - \varepsilon_{\mathrm{F}})|\psi_i(\mathbf{r})|^2 \qquad [9]$$

with $f(x)$ being the Fermi–Dirac distribution and ε_{F} the Fermi energy fixed by the condition

$$\int n(\mathbf{r})\mathrm{d}\mathbf{r} = N \qquad [10]$$

These are the famous KS equations; they must be solved self-consistently because V_{KS} is a functional of the orbitals itself. The generalization to finite temperature is obtained by replacing E with the electronic free energy $U = E - TS$, where S is the electronic entropy, given by the independent-electron formula $S = -2k_{\mathrm{B}}T\sum_i[f_i \ln f_i + (1-f_i)\ln(1-f_i)]$ with f_i being the thermal (Fermi–Dirac) occupation number of orbital i.

It is tempting to identify the single-particle eigenvalues ε_i with the energy of quasiparticles and therefore their distribution with the electronic density of states of the system. This would be conceptually wrong, as the KS eigenvalues are only an artificial mathematical tool to arrive at the ground-state density of the system. Nevertheless, it turns out that these DFT density of states often resemble very accurately the real density of states of systems, and they are therefore often used to analyze their electronic structure. However, it is important to remember that even if the exact XC functional $E_{\mathrm{xc}}[n]$ were known, one should not expect the DFT density of states to be an exact representation of the real density of states of the system.

When self-consistency is achieved, the electronic free energy of the system is

$$U = \sum_{i=1}^{N} f(\varepsilon_i - \varepsilon_{\mathrm{F}})\varepsilon_i - \frac{1}{2}\int \frac{n(\mathbf{r})n(\mathbf{r}')}{|\mathbf{r}-\mathbf{r}'|}\mathrm{d}\mathbf{r} + E_{\mathrm{xc}}[n]$$
$$- \int V_{\mathrm{xc}}(\mathbf{r})n(\mathbf{r})\mathrm{d}\mathbf{r} + E^{\mathrm{ion}} - TS \qquad [11]$$

where E^{ion} is the ionic electrostatic repulsion term. This would be the exact electronic free energy of the system if we knew $E_{\mathrm{xc}}[n]$ (which also depends on temperature, though very little is known about this dependence). Unfortunately, the exact form of the XC (free) energy is not (yet) known.

2.15.2.1.1   Exchange correlation functionals

Kohn and Sham (1965) also provided an approximate expression for the XC functional, called the LDA. In the LDA, the dependence of functional on the density has the form

$$E_{\mathrm{xc}}^{\mathrm{LDA}}[n] = \int n(\mathbf{r})\varepsilon_{\mathrm{xc}}(n(\mathbf{r}))\mathrm{d}\mathbf{r} \qquad [12]$$

and $\varepsilon_{\mathrm{xc}}(n)$ is taken to be the XC energy per particle of a uniform electron gas whose density is $n(\mathbf{r})$. This has been accurately calculated using Monte Carlo simulations (Ceperley and Alder, 1980) and parameterized in order to be given in an analytic form (Perdew and Zunger, 1981).

By construction, this approximation yields exact results if the density of the system is uniform and should not be very accurate for those systems whose density is highly dishomogeneous, for example, atoms and molecules. However, it turns out to work better than expected for a wide range of materials. In molecules, for example, the LDA usually overestimates the binding energies, but it yields in general good results for equilibrium distances and vibrational frequencies. It was the evidence of the very high quality of the LDA that has been the main responsible for the tremendous success of DFT.

Nowadays, a number of sophisticated functionals, like the so-called generalized gradient approximation (GGA) (e.g., Wang and Perdew, 1991) or the recently developed metaGGA (Staroverov et al., 2004; Tao et al., 2003), and hybrid functionals that contain a certain fraction of exact exchange according to various recipes (e.g., the B3LYP functional; Becke, 1993) have become available, but it is not obvious which one to prefer in general, with the good old LDA itself being competitive in accuracy in a variety of cases. It is also worth mentioning that, when used in combination with plane-waves methods (see Section 2.15.2.1.2), XC hybrid functionals usually require a computational effort that is orders of magnitudes higher than what is required by local XC functionals like the LDA or the GGAs. One of the main problems often ascribed to DFT is that it is difficult to incorporate dispersion interactions. Significant effort has been put in the last few years to correct XC functionals by adding dispersion corrections (e.g., Grimme, 2011; Tkatchenko et al., 2010 and references therein) or by developing new nonlocal functionals, which include dispersion interactions in the correlation energy (e.g., Lee et al., 2010; Klimeš et al., 2011 and references therein).

Whatever functional is used, these types of calculations all go under the classification of ab initio, in the sense that no experimental input is allowed, apart from the four fundamental constants mentioned in the preceding text. Of course, it would be desirable to have a unique functional with the highest possible accuracy for any system, but at the time of writing, we are not at this stage yet.

2.15.2.1.2   PPs and basis sets

In practical cases, it is often necessary to introduce one additional approximation in order to speed up the calculations, known as the PP approximation. In essence, this is a way to freeze the electrons of the core of the atoms and remove them from the calculations. The justification for doing this is that the core electrons are so tightly bound to the nuclei that they are essentially undisturbed by the chemical bonding, or

conversely, the chemistry of materials is unaffected by the behavior of the core electrons. This implies a saving in complexity and computer time, which is proportional to the number of electrons that have been frozen, but as we shall see in a moment, the saving becomes enormous in the most widely available computer codes, which are based on plane-wave expansions of the single-particle KS orbitals.

In order to solve the KS equations, it is necessary to expand the auxiliary KS orbitals in terms of some known basis functions. A variety of possible choices are available. Traditional quantum chemistry codes often use Gaussians, which are quite well suited for very localized orbitals, and in the course of the years, a large amount of expertise has accumulated to create high-quality basis sets for a wide range of materials. The drawback of Gaussians is that the quality of the basis set depends on the choice of the user, and transferability can be an issue when different systems are compared. An alternative set of functions, which are totally unbiased and systematically improvable, are plane waves. They also have the additional advantage of adapting naturally to calculations in which periodically boundary conditions are employed, which is a very useful set up even in systems, which have no periodicity, in order to reduce finite size effects. Plane-wave calculations are relatively simple, and the evaluation of forces and stress tensor is not much more difficult than the evaluation of the total energy. A drawback of plane waves is that a large number of them may be needed for describing rapidly varying functions, like the very localized core orbitals or the valence wave functions in the core region, which need to oscillate widely in order to be orthogonal to the core orbitals. For this reason, plane-wave calculations are almost always associated with the use of PPs.

The first aim of PPs is to eliminate the core electrons from the explicit calculations because they do not participate to the chemical properties of matter, at least until their binding energy is much higher than the energy involved in the chemical properties one wants to study. Hence, one freezes them around the nuclei and redefines the system as it was formed by ions plus valence electrons. We are left now with the problem of dealing with the oscillations in the core region of the valence wave functions, due to the orthogonalization to the core wave functions. The solution to this is the introduction of a PP, which substitutes the ionic Coulomb potential in such a way that the valence pseudoeigenvalues are the same as the all-electron (AE) ones on some reference configuration in the atom. The pseudo-wave functions coincide with the AE from a fixed core radius on and are as smooth as possible below the core radius, with the only constraint to be normalized (norm-conserving (NC) PPs). To satisfy these requirements, the PP usually must be angular momentum-dependent, that is, pseudo-wave functions corresponding to different angular momenta are eigenfunctions of different potentials. However, the long-range behavior of these different potentials must resemble the true one, because above the core radius, the pseudo-wave functions are identical to the AE ones. This mean that the difference must be confined in the core region and then the PP can be written in the following form (Bachelet et al., 1982; Hamann et al., 1979; Kerker, 1980):

$$V_a(\mathbf{r}, \mathbf{r}') = V_a^{\mathrm{loc}}(r)\delta(\mathbf{r} - \mathbf{r}') + \sum_{l=0}^{l_{\mathrm{max}}} V_{a,l}(r)P_l(\hat{\mathbf{r}}, \hat{\mathbf{r}}')\delta(r - r') \quad [13]$$

where $V_a^{\mathrm{loc}}(r)$ is the local long-range (spherical) part and approaches the AE potential above a cutoff radius $r_{\mathrm{c}}^{\mathrm{loc}}$, $V_{a,l}(r)$ are the short-range angular momentum-dependent part, the index a indentifies the atom, and P_l is the projector onto the angular momentum l,

$$P_l(\hat{\mathbf{r}}, \hat{\mathbf{r}}') = \sum_{m=-l}^{l^*} Y_{l,m}(\theta, \phi)Y_{l,m}^*(\theta', \phi') \quad [14]$$

with $Y_{l,m}$ being the spherical harmonics. The quality of the PP depends on its transferability properties, that is, the ability to reproduce the AE results over a wide range of electronic configurations, and of course the atom in different environments.

2.15.2.1.3 Ultrasoft (Vanderbilt) PPs

The requirement of norm conservation for the pseudo-wave functions can be a limiting factor for numerical calculations when also the valence electrons are very localized around their nuclei. This is a particularly serious problem for first-row elements, like carbon, and more so for nitrogen and oxygen and for transition metals, where the d-electrons are as localized as shallow-core states but have an extraction energy, which is not much larger than valence energies and for this reason cannot be excluded from the calculations. If this is the case, the utilization of NC PPs requires huge PW basis sets to achieve an acceptable accuracy. In a work published in 1990, Vanderbilt (1990) showed that, introducing a generalized formalism, the norm conservation constraint could be removed. In this way, one can construct much smoother pseudo-wave functions, with the only constraint of matching the AE at and above a fixed core radius (see Figure 1). The price to pay for having such smooth pseudo-wave functions is that, due to the fact that the pseudo-wave functions are not normalized anymore, the charge density has to be restored by adding an 'augmentation' part

$$n(\mathbf{r}) = \sum_i |\phi_i(\mathbf{r})|^2 + n_{\mathrm{aug}}(\mathbf{r}) \quad [15]$$

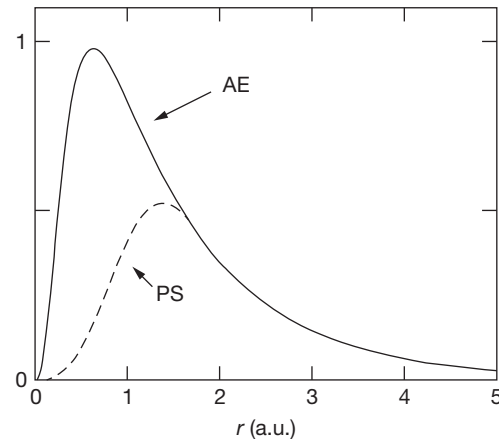and the KS equations take the generalized form

Figure 1 All-electron (solid) and ultrasoft pseudo (dashed)-radial wave functions of the 3d orbital of nickel. $r_{\mathrm{c}} = 1.75$ a.u.

$$H_{KS}|\phi_i\rangle = \varepsilon_i S|\phi_i\rangle \qquad [16]$$

where S is a nonlocal overlap operator.

2.15.2.1.4 The projector augmented wave method

In 1994, Blöchl invented a method to reconstruct the AE wave function inside the core region (Blöchl, 1994). The method, called projected augmented wave (PAW), is closely related to Vanderbilt's ultrasoft pseudopotential method, as shown by Kresse and Joubert (1999), but has been shown to be capable of reproducing essentially the same results of AE calculations, effectively removing the PP approximation. The PAW method is still only available in a handful of computer codes, but as evidences of its advantages accumulate, we believe that it will become a standard method of DFT–PW calculations.

2.15.2.2 Beyond DFT

As the search for the 'divine' functional in DFT goes on, alternative methods to solve the many-body problem are being developed, like the dynamic mean field theory (Savrasov and Kotliar, 2003) and QMC (Foulkes et al., 2001). The QMC method is particularly attractive because it adapts very well to parallel computers. As the speed of single-processor units approaches their physical limits, it is conceivable that the direction of the future increase of computer power will be the increase of the number of processors, and therefore, Monte Carlo methods will develop naturally on these machines. At the time of writing, the fastest computers in the world (e.g., Titan at Oak Ridge National Laboratory) already have more than 0.5 million processors working in parallel. Very few methods are capable of exploiting parallelism at this level efficiently; QMC is one of them.

QMC methods have been amply described in reviews (Foulkes et al., 2001), including detailed descriptions of how to implement them in practice (Foulkes et al., 2001; Umrigar et al., 1993). In the next section, I will briefly introduce the method and remand the reader to these reviews for more details.

2.15.2.2.1 QMC methods

QMC methods encompass a number of different techniques to solve the many-body problem of a system of N interacting quantum particles. In what follows, we will briefly mention the variational Monte Carlo (VMC) and the diffusion Monte Carlo (DMC) methods.

The VMC method gives an upper bound to the exact ground-state energy E_0. Given a normalized trial wave function $\Psi_T(\mathbf{R})$, where $\mathbf{R} = (\mathbf{r}_1, \mathbf{r}_2, \ldots, \mathbf{r}_N)$ is a $3N$-dimensional vector representing the positions of N electrons, and denoting by $\hat{H}$ the many-electron Hamiltonian, the variational energy $E_v \equiv \langle \Psi_T | \hat{H} | \Psi_T \rangle \geq E_0$ is estimated by sampling the value of the local energy $E_L(\mathbf{R}) \equiv \Psi_T^{-1}(\mathbf{R})\hat{H}\Psi_T(\mathbf{R})$ with configurations $\mathbf{R}$, distributed according to the probability density $\Psi_T(\mathbf{R})^2$. Common trial wave functions are of the Slater–Jastrow type:

$$\Psi_T(\mathbf{R}) = D^\uparrow D^\downarrow e^J \qquad [17]$$

where $D^\uparrow$ and $D^\downarrow$ are Slater determinants of up-spin and down-spin single-electron orbitals and e^J is the so-called Jastrow factor, which is the exponential of a sum of one-body and two-body terms (and possibly higher-order terms). The Jastrow factor is a parameterized function of electron separation, designed to satisfy the cusp condition, that is, to counterbalance the divergence in the potential when two electrons become very close, with a corresponding divergence in the kinetic energy of opposite sign. The parameters in the Jastrow factor are varied to minimize the variance of the local energy E_L, which also results in a minimization of the local energy itself. Several additional trial wave functions have also been used, including a more general form of that defined in eqn [17] in which one uses a linear combination of more than one Slater determinant or antisymmetrized geminals (Casula and Sorella, 2003).

Because of the variational principle, VMC results are an upper bound of true energy, which is not available in VMC (unless, of course, the trial wave function is the exact many-body wave function).

The DMC method is designed to obtain the true ground-state properties of the system. The basic idea is to compute the evolution of the many-body wave function Φ by the time-dependent Schrödinger equation in imaginary time $-\partial\Phi/\partial t = (\hat{H} - E_T)\Phi$, where E_T is an energy offset. If we consider only the kinetic energy in the Hamiltonian, the equation is equivalent to a diffusion equation, which allows Φ to be regarded as a probability distribution represented by a population of diffusing walkers. The potential term in the Hamiltonian makes the time-dependent Schrödinger equation in imaginary time equivalent to a rate equation, which is associated to a birth–death process of walkers in regions of low–high potential energy, respectively. It can be shown that, by adjusting the energy offset E_T appropriately, in the limit of imaginary time going to infinity, the distribution of walkers converges to the ground-state many-body wave function, and therefore, in principle, the DMC scheme yields the exact ground-state energy. However, for fermion systems, there is a fundamental problem. This is that Φ changes sign as $\mathbf{R}$ varies, so that it can only be treated as a probability in regions of $\mathbf{R}$-space where it does not change sign. These regions and the nodal surfaces that define their boundaries have to be fixed by the introduction again of some trial wave function Ψ_T. The consequence of this is that the energy given by DMC is not the true ground-state energy, but again an upper bound because of the constraint that the nodal surface is that of Ψ_T. This gives rise to the so-called fixed-node error. The form of Ψ_T is usually the same as that used in VMC, and it is used to provide a starting point for DMC simulations.

An important issue in QMC simulations is the representation of the single-particle orbitals that make up Ψ_T. Much as in DFT, a number of different choices are possible, including Gaussians, plane waves, or B-splines (Alfè and Gillan, 2004a). The latter have the attractive feature of being intimately related to plane waves, sharing the properties of being unbiased and systematically improvable, but also being localized, a crucial property in QMC simulations.

It has also been shown recently that the evaluation and the storage of the trial wave function Ψ_T, often the most expensive part of the calculations, can be performed such that its cost scales linearly with the size of the system (Alfè and Gillan, 2004b; Manten and Lüchow, 2003; Roboredo and Williamson, 2005; Williamson et al., 2001), making the

so-called o(N)-QMC techniques promising candidates for calculations on very large systems in the future.

The fixed-node error is the only uncontrollable source of error in DMC calculations; however, for systems containing atoms heavier than those of the first row, it is necessary to use PPs. The reason is that, for a trial wave function of fixed quality, the variance of the energy is proportional to the energy itself. Since core electrons have large negative energies, the variance associated to the evaluation of this component of the energy would mask completely the relatively small energies due to the valence electrons, which are those involved in the chemical bonding. For this reason, it is customary to use PPs also in QMC calculations. The nonlocality that is essential in these PPs gives rise to unavoidable errors in DMC. The reason is that the diffusion equation with a nonlocal Hamiltonian contains a term that can change its sign as time evolves and therefore presents the same difficulties as the fermion sign problem. To avoid this difficulty, one introduces the so-called localization approximation, in which this problematic term is simply neglected. If the trial wave function Ψ_T is close to the true (fixed-node) ground-state wave function Ψ, then this approximation introduces an error, which is small and proportional to $(\Psi_T - \Psi)^2$. This error, however, is nonvariational, so it can decrease and increase the total energy. Some recent promising work has gone toward addressing this problem (Casula et al., 2005, 2010).

To summarize, provided that all sources of technical errors are kept under control, the only two sources of error in QMC calculations are the fixed-node approximation and the locality approximation. It has been shown that DMC techniques can deliver much higher accuracy than DFT techniques (Binnie et al., 2010; Filippi et al., 2002; Grossman et al., 1995; Leung et al., 1999; Pozzo and Alfè, 2008; Santra et al., 2011; Tkatchenko et al., 2012), hinting that the aforementioned two approximations are less serious than those involved in the formulation of XC functionals in DFT calculations (at least for the systems considered). However, DMC total energy calculations are typically 4 orders of magnitude more expensive than traditional DFT techniques, and for this reason, the range of materials studied so far is rather limited, and therefore, so is the evidence that would favor DMC compared to DFT. As mentioned already in the preceding text, however, QMC techniques adapt naturally to large parallel computers (Towler et al., 2011), while traditional DFT techniques can take less advantage of this kind of architecture. It is expected therefore that the development and application of QMC techniques will be boosted in the future.

2.15.3 Mineral Properties and Behavior

Having introduced the computational tools, I now turn the discussion to the main purpose of this chapter, namely, how these tools can be applied to the study of the high-pressure and high-temperature properties of materials. I will focus in particular on the structure and elastic properties, phase diagrams, phase transitions, and thermodynamics of solutions.

To simulate materials under pressure is not much more difficult than to perform calculations at zero pressure; all it needs to be done is to change the volume of the simulation cell appropriately. In doing so, one possible problem can be the shortening of the nearest-neighbor distance among the atoms, which, if it drops below the sum of the core radii of the PPs employed (or PAW-potentials), may affect the quality of the results. Therefore, some care is necessary in designing the potentials appropriate for the conditions where they need to be used. However, apart from this possible shortcoming, it is often the case that simulations at high pressure are even more accurate than those at low pressure. The reason is that as the pressure increases, the charge density becomes more homogeneous, which helps the XC functionals in their work.

By contrast, high-temperature simulations are much more demanding than the zero-temperature ones. The reason is that at high temperature, it is the free energy to play the essential role, and an accurate calculation of this requires expensive sampling of the phase space. For solids at not too high temperature, it is often accurate enough to use the quasi-harmonic approximation, in which the potential energy of the crystal is expanded to the second order in the displacement of the atoms away from their equilibrium positions. This quasi-harmonic potential usually provides a very accurate description of the dynamic properties of the system at low temperature and gives easy access to the free energy of the system, which can be calculated analytically as a function of temperature. The prefix 'quasi-' is there to indicate that this quasi-harmonic potential depends on the volume of the system. In practice, the quality of the thermodynamics obtained within the quasi-harmonic approximation is often preserved also to temperatures not far from the melting temperature, although at such high temperatures, a full account of anharmonic effects becomes necessary, at least to assess the validity of the quasi-harmonic approximation. For highly anharmonic solids and for liquids, one has to resort to MD or Monte Carlo techniques to sample the phase space. MD simulations are particularly attractive because they also provide dynamic information like diffusion or autocorrelation properties, which can be used together with the fluctuation–dissipation theorem to evaluate a number of physical properties of the system, as we shall see in the succeeding text. In the next section, we start by looking at the zero-temperature properties of materials, and in the following section, we turn to finite temperature.

2.15.3.1 Static Properties

2.15.3.1.1 Crystal structures and phase transitions

At zero temperature, the main thermodynamic variable is the internal energy of the system E. The simplest possible first-principles calculation one can do is the evaluation of the total energy of a system containing a certain number of atoms at fixed lattice sites. To find the most stable configuration of the atoms, one simply minimizes the total energy with respect to the atomic positions. This is usually done by evaluating forces, which are then used to move the atoms toward their equilibrium positions. For simple crystal structures, this could not be necessary, as the positions may be constrained by symmetry. An example of this is the Earth's mantle mineral MgO (periclase), which at zero pressure has a face-centered cubic crystal structure, with the Mg and O atoms in the primitive cell sitting at the corners and at the center of the
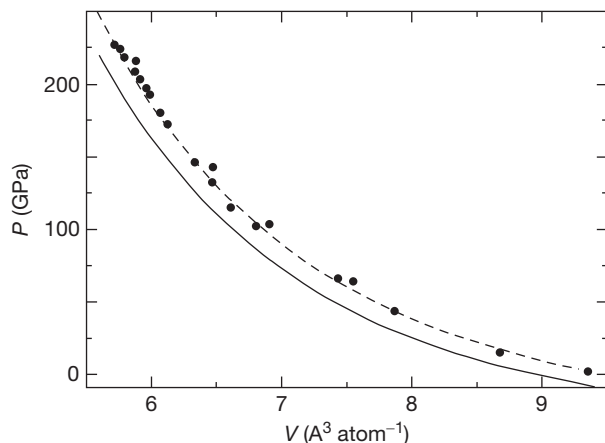
Figure 2 Pressure as function of atomic volume for rock salt MgO calculated with DFT–LDA (solid line) and DFT–GGA (dashed line), compared with experiments (stars) (Duffy et al., 1995). Calculations do not include zero-point or thermal effects. Reprinted from Alfè D (2005) *Physical Review Letters* 94: 235701, with permission. Copyright 2005 American Physical Society.

conventional cubic cell. In **Figure 2**, I show a comparison of pressures as function of volume between first-principles calculations and experiments. The calculations have been performed with DFT and both the LDA and the GGA approximations known as PW91 (Wang and Perdew, 1991) for the XC. The GGA results appear to agree very well with the experimental data, while the LDA one underestimates the pressure slightly. However, these particular calculations do not include zero-point motion and room temperature thermal expansion, which are instead present in the experiments. With those effects included (Karki et al., 2000), the experimental data would fall roughly in the middle of the two theoretical curves.

As the pressure is increased, the crystal structure of the material may change. For MgO, this does not happen up to at least 227 GPa (Duffy et al., 1995), but it is believed that as the pressure is increased still further, MgO would transform to the structure of CsCl, which is a simple cubic with the Mg and O atoms in the primitive cell still sitting at the corner and the center of the cube, respectively. The pressure at which the phase transformation occurs is defined by the point where the enthalpies of the two crystal structures cross. These enthalpies can be computed using ab initio techniques, by computing the energy E and the pressure p of the crystal as function of volume V, and then construct the enthalpy $H = E + pV$. For MgO, this has been done using a number of different techniques in the past, including various flavors of DFT (Chang and Cohen, 1984; Drummond and Ackland, 2002; Jaffe et al., 2000; Karki et al., 1997; Mehl et al., 1988; Oganov and Dorokupets, 2003; Oganov et al., 2003) and, very recently, QMC (Alfè et al., 2005). The latest DFT results point toward a transition at around 500 GPa, and the QMC results show that the transition is at 600 ± 30 GPa.

Another example of phase transition between different crystal structures is the transformation of iron from the zero-pressure magnetic body-centered cubic (bcc) to the hexagonal close-packed (hcp) structure at a pressure between 10 and

15 GPa (Jephcoat et al., 1986). Like the previous MgO case, the cubic structure is symmetrical, and it is necessary only to evaluate the energy of the crystal as function of volume. In contrast to bcc, however, the hcp crystal structure has an additional degree of freedom, coming from the lack of a symmetry relating the hexagonal plane and the direction perpendicular to the plane. This additional degree of freedom, known as the c/a ratio, needs to be optimized for every volume V. Once this is done, an enthalpy curve can be constructed and compared with that obtained from the bcc structure. Calculations using DFT with the LDA or various GGA's have been performed, and it has been shown that in this particular case, the LDA gives poor agreement with the experiments, even failing to predict the correct zero-pressure crystal structure (Cho and Scheffler, 1996; Körling and Häglund, 1992; Leung et al., 1991; Singh et al., 1991; Zhu et al., 1992), while PW91, for example, predicts the transition between 10 and 13 GPa (depending on the exact details of the pseudopotential or PAW potential) (Alfè et al., 2000a), in good agreement with the experimental value, which is in the range 10–15 GPa (Jephcoat et al., 1986).

Finally, as the last example, we mention the Earth's mantle mineral $MgSiO_3$ perovskite, which at mantle pressures has an orthorhombic crystal structure with the atoms in the cell not constrained by symmetry operations (D'Arco et al., 1993; Stixrude and Cohen, 1993; Wentzcovitch et al., 1993). It follows that at any fixed volume, one needs to optimize not only the lattice vectors but also the positions of the atoms in the cell. Very recently, this mineral has been found to display a phase transition to a new phase, named postperovskite (Murakami et al., 2004; Oganov and Ono, 2004). This transition has also been found by ab initio calculations (Iitaka et al., 2004; Oganov and Ono, 2004; Tsuchiya et al., 2004). The transition pressure from the static first-principles calculations appears to be $\sim$100 GPa, which is below the core–mantle mantle pressure. However, Oganov and Ono (2004) and Tsuchiya et al. (2004) showed that high-temperature harmonic effects are responsible for an increase in the transition pressure, which is therefore predicted to be close to that at the top of D″ zone at the bottom of the mantle.

2.15.3.1.2 Elastic constants

Most of what we know about the interior of our planet comes from seismology and therefore from the elastic behavior of the minerals inside the Earth. The theory of elasticity of crystals can be found in standard books (Wallace, 1998), and therefore, we will not dwell on it for too long. Briefly, if a crystal is subjected to an infinitesimal stress $d\sigma_{ij}$, with i and j running through the three Cartesian directions in space, then it will deform according to the strain matrix $d\varepsilon_{ij}$:

$$d\sigma_{ij} = \sum_{k,l} c_{ijkl} d\varepsilon_{kl} \qquad [18]$$

The constant of proportionality between stress and strain, C_{ijkl}, is a rank 4 tensor of elastic constants. With no loss of generality, we can assume $d\sigma_{ij}$ and $d\varepsilon_{ij}$ to be symmetrical ($d\sigma_{ij} \neq d\sigma_{ji}$ would imply a nonzero torque on the crystal, which would simply impose an angular acceleration and not a deformation), and therefore, the elastic constant tensor is also symmetrical. It is therefore possible to rewrite the rank 2 tensors $d\sigma_{ij}$ and $d\varepsilon_{ij}$ as six-component vectors, in the Voigt

notation, with the index pairs 11, 22, 33, 23, 31, and 12 represented by the six symbols 1, 2, 3, 4, 5, and 6, respectively. In this notation, the stress–strain relation appears as

$$d\sigma_i = \sum_j C_{ij} d\varepsilon_j \qquad [19]$$

with i and j going from 1 to 6. Elastic constants are given as the coefficients C_{ij} in this notation. The matrix C_{ij} is symmetrical, so that the maximum number of independent elastic constants of a crystal is 21. Because of crystal symmetries, the number of independent constants is usually much smaller. For example, in cubic crystals, there are only three elastic constants; in hcp Fe, there are five; and in orthorhombic $MgSiO_3$ perovskite, there are nine.

Equation [19] provides the route to the calculation of the elastic properties of materials, and it can be applied at both zero and high temperatures. At zero temperature, the components of stress tensor can be calculated as (minus) the partial derivative of the internal energy with respect to the components of the strain:

$$\sigma_{ij} = -\partial E / \partial \varepsilon_{ij}|_\varepsilon \qquad [20]$$

Examples of zero-temperature calculations of elastic constants include the DFT calculations of Stixrude and Cohen (1995) on the hcp crystal structure of iron at the Earth's inner-core conditions, which suggested a possible mechanism based on the partial alignment of hcp crystallites to explain the seismic anisotropy of the Earth's inner core. Other examples are the recent GGA and LDA calculations of the elastic constant of the recently discovered postperovskite phase by three groups (Iitaka et al., 2004; Tsuchiya et al., 2004; Oganov and Ono, 2004; Oganov et al., 2005), which showed that this phase is elastically very anisotropic and that with a proper alignment, it is possible to explain the observed seismic anisotropy of the D″ region.

2.15.3.2 Finite Temperature

The extension to finite-temperature properties of materials could simply be obtained by substituting the internal energy E with the Helmholtz free energy F. The ij component of the stress tensor σ_{ij} is (minus) the partial derivative of F with respect to strain ε_{ij}, taken at constant T, and holding all the other components of the strain tensor constant,

$$\sigma_{ij} = -\partial F / \partial \varepsilon_{ij}|_{\varepsilon, T} \qquad [21]$$

Similarly, the pressure p is obtained as (minus) the partial derivative of F with respect to volume, taken at constant temperature:

$$p = -\partial F / \partial V|_T \qquad [22]$$

If the system of interest is at sufficiently high temperature (above the Debye temperature), the nuclei can be treated as classical particles, and the expression of the Helmholtz free energy F for a system of N identical particles enclosed in a volume V and in thermal equilibrium at temperature T is (Frenkel and Smit, 1996)

$$F = -k_B T \ln \left\{ \frac{1}{N! \Lambda^{3N}} \int_V d\mathbf{R}_1 \ldots d\mathbf{R}_N e^{-\beta U(\mathbf{R}_1, \ldots, \mathbf{R}_N; T)} \right\} \qquad [23]$$

where $\Lambda = h/(2\pi M k_B T)^{1/2}$ is the thermal wavelength, with M being the mass of the particles and h being the Plank's constant; $\beta = 1/k_B T, k_B$ is the Boltzmann constant; and $U(\mathbf{R}_1, \ldots, \mathbf{R}_N; T)$ is the potential energy function, which depends on the positions of the N particles in the system and possibly on temperature, in which case U is the electronic free energy. The multidimensional integral extends over the total volume of the system V.

By taking (minus) the derivative of F with respect to volume at constant temperature, we obtain

$$p(V, T) = \frac{N k_B T}{V} + \frac{\int_V d\mathbf{R}_1 \ldots d\mathbf{R}_N e^{-\beta U(\mathbf{R}_1, \ldots, \mathbf{R}_N; T)} \left(\frac{-\partial U(\mathbf{R}_1, \ldots, \mathbf{R}_N; T)}{\partial V} \right)_T}{\int_V d\mathbf{R}_1 \ldots d\mathbf{R}_N e^{-\beta U(\mathbf{R}_1, \ldots \mathbf{R}_N; T)}}$$

$$= \frac{N k_B T}{V} + \left\langle \left(\frac{-\partial U(\mathbf{R}_1, \ldots \mathbf{R}_N; T)}{\partial V} \right)_T \right\rangle \qquad [24]$$

The first term is the kinetic pressure and is present also in a system with no interactions between the particles (the ideal gas). The appearance of this term can be also understood by realizing that the integral appearing in eqn [23] is proportional to V^N. The second term is the canonical thermal average of the derivative of the potential (free) energy function with respect to volume, taken at constant temperature.

A similar expression holds for the stress tensor, which at finite temperature is evaluated as the thermal average of the derivative of F with respect to the strain components, plus the kinetic term.

Analogously, the internal energy $E = (\partial (F/T) / \partial (1/T))_V$ is given by

$$E(V, T) = \frac{3}{2} N k_B T + \langle U(\mathbf{R}_1 \ldots \mathbf{R}_N; T) \rangle \qquad [25]$$

This shows that a number of finite properties can simply be calculated by taking the thermal average of the corresponding quantity evaluated at $T = 0$, plus a trivial kinetic term.

2.15.3.2.1 Molecular dynamics

If the system is ergodic, thermal averages (represented in the equations in the preceding text) can be calculated as time averages along an MD simulation (Alder and Wainwright, 1959; Gibson et al., 1960). The main idea here is to move the ions according to the Newton's equations of motion. This is achieved in practice by discretizing the equation of motion $m_i \partial \mathbf{v}_i / \partial t = \mathbf{F}_i$ (m_i is the mass of atom i, $\mathbf{v}_i$ is its velocity, and $\mathbf{F}_i$ is the force acting on it). This is done by dividing time into time steps Δt and approximating the solution of the equation of motion, for example, as proposed by Verlet (Allen and Tildesley, 1987; Frenkel and Smit, 1996; Verlet, 1967):

$$\mathbf{r}_i(t + \Delta t) = 2\mathbf{r}_i(t) - \mathbf{r}_i(t - \Delta t) + \frac{1}{m_i} \mathbf{F}_i(t) \Delta t^2 + o(\Delta t^4)$$

$$\mathbf{v}_i(t) = \frac{\mathbf{r}_i(t + \Delta t) - \mathbf{r}_i(t - \Delta t)}{2\Delta t} + o(\Delta t^3) \qquad [26]$$

If the time step is small enough (usually less than 1/20 of a typical vibrational period), the Verlet algorithm conserves well the total energy of the system, on both short and long time-scales. If the volume of the simulation cell V and the number of

atoms N are kept constant, this so-called (N, V, E) simulation generates configurations in phase space that are distributed according to the microcanonical ensemble.

It is a standard result of statistical mechanics that thermal averages evaluated either in the microcanonical ensemble or in the canonical ensemble are equivalent if the system is sufficiently large, but it is useful to be able to perform simulations in ensembles other than the microcanonical one. For example, in order to obtain thermal averages in the canonical ensemble (i.e., constants N, V, and T), like the pressure in eqn [24], one can couple the system with an external heat bath, following the prescription of Andersen (Andersen, 1980), Nosé, or Hoover (Nosé, 1984; Hoover, 1985). When combined with the Parrinello–Rahman constant-stress technique (Parrinello and Rahman, 1980), this also allows simulations to be performed at constant T and $\sigma_{\alpha\beta}$ (see, e.g., Wentzcovitch et al. (1993)).

The forces F_i can be calculated within the framework of DFT, in which case the method is sometimes called first-principles molecular dynamics (FPMD). As mentioned earlier, for the method to be applicable in practice, one makes the fundamental approximation that the dynamics of the ions is decoupled from that of the electrons. This is usually justified due to the large difference in masses between the two sets of particles.

The first FPMD simulation was performed by Car and Parrinello (CP) in 1985 (Car and Parrinello, 1985), who proposed an elegant method to keep the electrons on the ground state along the MD trajectory. This was done by including the electronic degrees of freedom into a generalized Lagrangian, by assigning a fictitious mass to the single-particle wave functions and treating them as dynamic variables, like the positions of the ions. With a judicious choice of this fictitious mass, the electronic degrees of freedom would remain decoupled from the ionic ones, following them adiabatically while remaining in the their ground state (at least for nonmetallic systems). An alternative method is to bring the electrons to the ground state at each time step (Kresse and Furthmuller, 1996), which is usually more costly than the CP scheme, but this is compensated by the possibility of making longer time steps. This method can be also easily applied to metallic systems and can become very efficient if combined with the extrapolation of the single-particle wave functions (Arias et al., 1992; Mead, 1992) and the electronic charge density (Alfè, 1999).

As some examples of the use of FPMD to compute thermal averages and study the high-temperature properties of solids, we mention the work of Oganov et al. (2001), who studied the high-temperature elastic constants of $MgSiO_3$ perovskite, and more recently that of Wookey et al. (2005), who studied the high-temperature elastic constants of $MgSiO_3$ postperovskite, and Gannarelli et al. (2005), who studied the elastic behavior of hcp iron at inner-core p and T conditions.

Using MD simulations, it is also possible to study the properties of liquids. For example, in a liquid, the atoms are free to diffuse throughout the whole volume, and this behavior can be characterized by diffusion coefficients D_α, where α runs over different species in the system. These D_α are straightforwardly related to the mean square displacement of the atoms through the Einstein relation (Allen and Tildesley, 1987):

$$\frac{1}{N_\alpha}\left\langle \sum_{i=1}^{N_\alpha} |\mathbf{r}_{\alpha i}(t_0 + t) - \mathbf{r}_{\alpha i}(t_0)|^2 \right\rangle \rightarrow 6D_\alpha t, \text{ as } t \rightarrow \infty \qquad [27]$$

where $\mathbf{r}_{i\alpha}(t)$ is the vector position at time t of the ith atom of species α, N_α is the number of atoms of species α in the cell, and $\langle\ \rangle$ means time average over t_0. The diffusion coefficient can also be used to obtain a rough estimate of the viscosity η of the liquid, by using the relation between the two stated by the Stokes–Einstein relation:

$$D\eta = \frac{k_B T}{2\pi a} \qquad [28]$$

This technique was used by de Wijs et al. (1998) to estimate the viscosity of liquid iron at the Earth's core conditions. The Stokes–Einstein relation [28] is exact for the Brownian motion of a macroscopic particle of diameter a in a liquid of viscosity η. The relation is only approximate when applied to atoms; however, if a is chosen to be the nearest neighbors distance of the atoms in the solid, eqn [28] provides results that agree within 40% for a wide range of liquid metals. To calculate the viscosity rigorously, it is possible to use the Green–Kubo relation:

$$\eta = \frac{V}{k_B T} \int_0^\infty dt \langle \sigma_{xy}(t)\sigma_{xy}(0) \rangle \qquad [29]$$

where σ_{xy} is the off-diagonal component of the stress tensor $\sigma_{\alpha\beta}$ (α and β are Cartesian components). This relation was used in the context of first-principles calculations for the first time by Alfè and Gillan (1998b), who first calculated the viscosity of liquid aluminum at ambient pressure and a temperature of 1000 K, showing that the method provided results in good agreement with the experiments and then applied the method to the calculation of the viscosity of a liquid mixture of iron and sulfur under the Earth's core conditions. In Figure 3, I show the integral in eqn [29] calculated from 0 to time t for this iron sulfur liquid mixture. In principle, this has to be
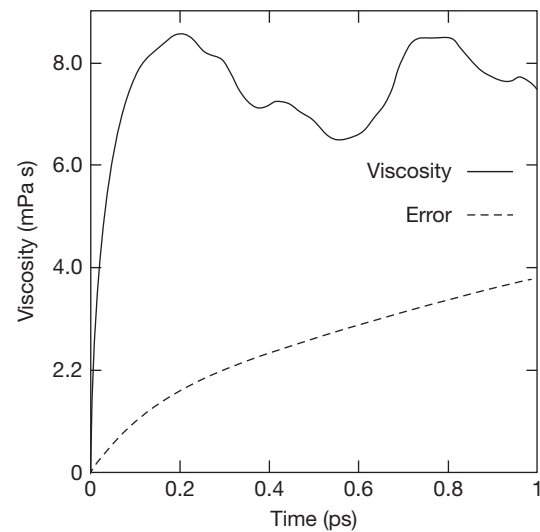

Figure 3 Viscosity integral of the average stress autocorrelation function and its statistical error as a function of time for liquid Fe/S under the Earth's core conditions. Reprinted from Alfè D and Gillan MJ (1998) *Physical Review Letters* 81, with permission. Copyright 1998 American Physical Society.

computed from zero to infinity, as stated in eqn [29]; however, in this particular case, there is nothing to be gained by extending the integral beyond about 0.2 ps, after which the integrand has decayed to zero and it is dominated by statistical noise. The figure also shows the computed statistical error on the integral, and from this, it was possible to infer the value for the viscosity $\eta = 9 \pm 2$ mPa s, in good agreement with that obtained from the diffusion coefficient via the Einstein relation [28], calculated to be $\eta \sim 13$ mPa s in a previous paper (Alfè and Gillan, 1998a).

2.15.3.3 Thermodynamic Properties

The phase stability of a system is determined by the minimum of its Gibbs free energy $G = F + pV$. Since $p = -\partial F/\partial V|_T$, knowledge of F as function of V and T allows the computation of G.

More generally, equilibrium in a multispecies system is determined by the chemical potentials μ_i, with i running over the different species, which represents the constant of proportionality between the energy of the system and the amount of the species i (Wannier, 1966):

$$\mu_i = \left(\frac{\partial E}{\partial N_i} \right)_{S,V} \qquad [30]$$

where S is the entropy and N_i is the number of particles of the species i. Alternative equivalent definitions of the chemical potential are (Wannier, 1966; Mandl, 1997)

$$\mu_i = \left(\frac{\partial F}{\partial N_i} \right)_{T,V} = \left(\frac{\partial G}{\partial N_i} \right)_{T,p} = -T \left(\frac{\partial S}{\partial N_i} \right)_{E,V} \qquad [31]$$

Equilibrium between two phases is determined by the condition of equality of the chemical potential of each individual species in the two phases. In the next section, I start the discussion by considering a single-component system. The extension to multicomponent systems will be considered in Section 2.15.3.3.5.

2.15.3.3.1 The Helmholtz free energy: Low temperature and the quasi-harmonic approximation

For a solid at low temperature, F can be easily accessed by treating the system in the quasi-harmonic approximation. This is obtained by expanding the potential (free) energy function U around the equilibrium positions of the nuclei. The first term of the expansion is simply the energy of the system calculated with the ions in their equilibrium positions, $E_{\text{perf}}(V, T)$ (this is a free energy at finite temperature, because of electronic entropy, and therefore depends on both V and T). If the crystal is in its minimum energy configuration, the linear term of the expansion is zero, and by neglecting terms of order three and above in the atomic displacements, we have that the quasi-harmonic potential is

$$U_{\text{harm}} = E_{\text{perf}} + \frac{1}{2} \sum_{ls\alpha, l't\beta} \Phi_{ls\alpha, l't\beta} u_{ls\alpha} u_{l't\beta} \qquad [32]$$

where u_{ls} denotes the displacement of atom s in unit cell l, α and β are Cartesian components, and $\Phi_{ls\alpha, l't\beta}$ is the force-constant matrix, given by the double derivative $\partial^2 U/\partial u_{ls\alpha} \partial u_{l't\beta}$ evaluated with all atoms at their equilibrium positions. This force-constant matrix gives the relation between the forces $\mathbf{F}_{ls}$

and the displacements $\mathbf{u}_{l't}$, as can be seen by differentiating eqn [32]:

$$F_{ls\alpha} = -\partial U/\partial u_{ls\alpha} = -\sum_{l't\beta} \Phi_{ls\alpha, l't\beta} u_{l't\beta} \qquad [33]$$

Within the quasi-harmonic approximation, the potential energy function U_{harm} completely determines the physical properties of the system, and in particular the free energy, which takes the form

$$F(V, T) = E_{\text{perf}}(V, T) + F_{\text{harm}}(V, T) \qquad [34]$$

where the quasi-harmonic component of the free energy is

$$F_{\text{harm}} = k_B T \sum_n \ln \left(2 \sinh \left(\hbar w_n / 2 k_B T \right) \right) \qquad [35]$$

with w_n being the frequency of the nth vibrational mode of the crystal. In a periodic crystal, the vibrational modes can be characterized by a wave vector $\mathbf{k}$, and for each such wave vector, there are three vibrational modes for every atom in the primitive cell. If the frequency of the sth mode at wave vector $\mathbf{k}$ is denoted by $w_{\mathbf{k}s}$, then the vibrational free energy is

$$F_{\text{harm}} = k_B T \sum_{\mathbf{k}s} \ln \left(2 \sinh \left(\hbar w_{\mathbf{k}s} / 2 k_B T \right) \right) \qquad [36]$$

The vibrational frequencies $w_{\mathbf{k}s}$ can be calculated from first principles, and we shall see in the succeeding text how this can be done.

Once this quasi-harmonic free energy is known, all the thermodynamic properties of the system can be calculated. In particular, the pressure is given by

$$p = -\partial F/\partial V|_T = -\partial E_{\text{perf}}/\partial V|_T - \partial F_{\text{harm}}/\partial V|_T \qquad [37]$$

The last term in the equation in the preceding text is the ionic component of the thermal pressure, and it is different from zero because the vibrational frequencies $w_{\mathbf{k}s}$ depend on the volume of the crystal. In fact, it is easy to see from eqn [36] that even at zero temperature, there is a finite contribution to the quasi-harmonic free energy, given by

$$F_{\text{harm}}(V, 0) = \sum_{\mathbf{k}s} \frac{\hbar w_{\mathbf{k}s}}{2} \qquad [38]$$

This zero-point energy contribution to the harmonic free energy is also responsible for a contribution to the pressure. Since usually the vibrational frequencies $w_{\mathbf{k}s}$ increase with decreasing volume, these contributions are positive and are responsible for the phenomenon of thermal expansion in solids.

The dependence of $E_{\text{perf}}(V, T)$ on T also means that there is an electronic contribution to the thermal pressure, which is also positive, and in some cases (i.e., iron at Earth's core conditions) can be a significant fraction of the thermal pressure and a nonnegligible fraction of the total pressure (Alfè et al., 2001).

As an example of a calculation of the thermal expansivity of minerals using the quasi-harmonic approximation, I show in Figure 4 the temperature dependence of the thermal expansivity α of MgO at pressures up to 200 GPa, compared with experimental results. At ambient pressure, the first-principles $\alpha(T)$ agrees very closely with experiment up to ~ 1000 K (about

one-third of the melting temperature), which is a result of the good agreement of the calculated phonons with the experimental ones. The increasingly poor agreement at high T is due to anharmonic effects coming into play. These can be taken into account by avoiding the quasi-harmonic approximation and evaluating the full free energy of the system, as we shall see in Section 2.15.3.3.3.

2.15.3.3.2   Calculation of phonon frequencies

There are two different first-principles strategies for calculating phonon frequencies. The method that is easier to understand starts from the fact that the force-constant matrix expresses the proportionality between displacements and forces, when the displacements are small enough for this relationship to be linear. All that has to be done in principle is to displace a single atom t in cell l' in Cartesian direction β, all other atoms being held fixed at their equilibrium positions; the forces $F_{ls\alpha}$ on all the atoms then give directly the elements of the force-constant matrix $\Phi_{ls\alpha,l't\beta}$ for the given $(l't\beta)$. If this procedure is repeated for all other $(l't\beta)$, all the elements of the force-constant matrix can be obtained. Translational invariance implies that the number of separate calculations required to do this is at most three times the number of atoms in the primitive cell, but for most materials, symmetry relations can be used to reduce this number substantially. This strategy, sometimes called the small displacement method (Kresse et al., 1995), is implemented, for example, in the PHON code (Alfè, 2009a). Although the small displacement method is widely used and can be very accurate, a word of caution is in order. Since DFT calculations on condensed matter always use periodic boundary conditions, the repeating cell must be large enough so that the elements $\Phi_{ls\alpha,l't\beta}$ have all fallen off to negligible values at the boundary of the repeating cell. This is readily achieved for some materials, particularly metals. However, in ionic materials, the force-constant elements fall off only as r^{-3}, and convergence can be slow. Moreover, in polar materials, the Coulomb forces produce a macroscopic electric field in the limit of zero wave vector. This electric field is responsible for a splitting in the frequencies of the vibrational modes parallel and perpendicular to the electric field (the so-called LO–TO splitting). This effect can be taken into account by adding a nonanalytic contribution to the dynamic matrix at wave vector $\mathbf{k}$, which has the form (Giannozzi et al., 1991)

$$D_{s\alpha,t\beta}^{\mathrm{na}} = (m_s m_t)^{-1/2} \frac{4\pi e^2}{\Omega} \frac{\left(\mathbf{k}Z_s^*\right)_\alpha \left(\mathbf{k}Z_t^*\right)\beta}{\mathbf{k}\varepsilon^\infty \mathbf{k}} \qquad [39]$$

where Z_s^* is the Born effective charge tensor for atom s, ε^∞ the high-frequency static dielectric tensor, and m_s, m_t the mass of the atoms. These two quantities can be calculated in the framework of density functional perturbation theory (Baroni et al., 1987, 2001; Giannozzi et al., 1991) (DFPT), which also provides a second elegant strategy for the calculation of phonons in crystals. The main idea in DFPT, pioneered by Baroni et al. (1987), is to exploit the Hellmann–Feynman theorem to show that a linear order variation in the electron density upon application of a perturbation to the crystal is responsible for a variation in the energy up to second (in fact, third (Gonze and Vigneron, 1989)) order of the perturbation. Using the standard perturbation theory, this linear order variation of the electronic charge density can be calculated using only unperturbed wave functions, which therefore only require calculations on the ground-state crystal. If the perturbation is a phonon wave with wave vector $\mathbf{k}$, calculation of the density change to linear order in the perturbation can be used to determine the force-constant matrix at wave vector $\mathbf{k}$. This can be done for any arbitrary wave vector, without the need of the construction of a supercell. The implementation of the method is by no means straightforward, and for further details, the reader should consult the original papers (Baroni et al., 1987; Giannozzi et al., 1991).

It should be pointed out, however, that free energies computed with the small displacement method converge very quickly to the thermodynamic limit with the size of the supercell, as demonstrated for the case of MgO in Alfè (2009a), even when LO–TO splitting is ignored. An additional advantage of the small displacement method is that it only requires the computation of forces and therefore does not need to be integrated into a first-principles code. Moreover, for large unit cells, the small displacement method is usually more efficient than DFPT.

As an example of first-principles calculations of phonon frequencies using the small displacement method (Alfè, 2009a), I show in Figure 5 the phonon dispersion relations for bcc iron under ambient conditions, compared with experimental data. We see that the agreement between theory and experiments is very good almost everywhere in the Brillouin zone, with discrepancies being at worst ~3%.

Phonons can also be calculated at high pressure, and as an illustration of this, in Figure 6, I show a comparison between DFT–GGA-calculated phonons, using the small displacement method (Alfè, 2009a), and nuclear resonant inelastic x-ray scattering (NRIXS) (Seto et al., 1995; Sturhahn et al., 1995)

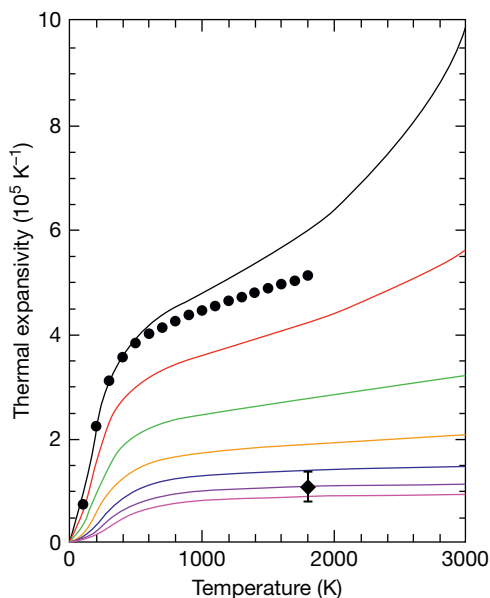**Figure 4**   Temperature dependence of thermal expansivity α of MgO on isobars at 0, 10, 30, 60, 100, 150, and 200 GPa (curves from top to bottom). Experimental data at zero pressure are indicated by filled circles. Average value of α over temperature range of 300–3300 K and pressure range of 169–196 GPa derived from shock-wave experiments is indicated by the diamond.
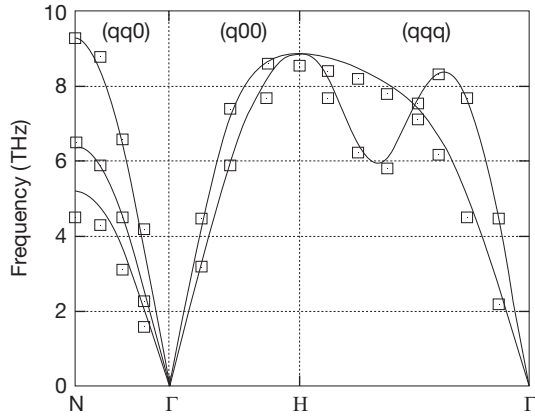
Figure 5 Phonon dispersion relations of ferromagnetic b.c.c. Fe. Lines and open squares show first-principles theory and experiment, respectively. Reproduced from Alfè D, Kresse G, and Gillan MJ (2000) *Physical Review B* 61: 132, with permission. Copyright 2000 American Physical Society.
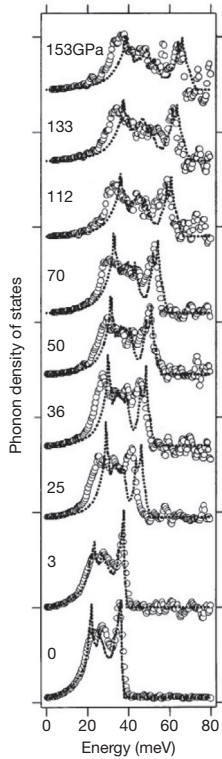

Figure 6 Phonon density of states of b.c.c. Fe (pressure $p=0$ and 3 GPa) and h.c.p. Fe (p from 25 to 153 GPa). Dotted curves and open circles show first-principles theory and experiment, respectively.

experiments, of phonon density of states of bcc and hcp iron from 0 to 153 GPa (Mao et al., 2001). The agreement between theory and experiments is good in the whole pressure region, being slightly better at high pressure.

The NRIXS technique has also been recently used to measure the partial density of states of FeS as a function of pressure (Kobayashi et al., 2004). Measurements were taken at pressures

of 1.5, 4.0, and 9.5 GPa, in the troilite, MnP-type, and monoclinic crystal structures of FeS, respectively, and were compared with first-principles calculations based on DFT–GGA. The agreement between the calculations and the experiments was reasonably good, although the FeS in the troilite structure was found to be unstable. The calculations were also used to provide the total density of states, which provided thermodynamic quantities such as the entropy and the specific heat.

2.15.3.3.3 The Helmholtz free energy: High temperature and thermodynamic integration

At high temperature, anharmonic effects in solids may start to play an important role, and the quasi-harmonic approximation may be not accurate enough. Moreover, if the system of interest is a liquid, the quasi-harmonic approximation is of no use. In this section, I shall describe a method to calculate the free energy of solids and liquid in the high temperature limit, provided that the temperature is high enough that the quantum nature of the nuclei can be neglected. If this is the case, the Helmholtz free energy F is defined as in eqn [23].

Performing the integral in eqn [23] to calculate F is extremely difficult. However, it is less difficult to calculate changes in F as some specific variables are changed in the system. For example, we have seen that by taking the derivative of F in eqn [23] with respect to volume at constant T, we obtain (minus) the pressure. Therefore, the difference of F between two volumes can be obtained by integrating the pressure p, which can be calculated using an MD simulation. Similarly, by integrating the internal energy E, one obtains differences in F/T.

It is equally possible to calculate differences in free energy between two systems having the same number of atoms N, the same volume V, but two different potential energy functions U_0 and U_1. This can be done by introducing an intermediate potential energy function U_λ such that for $\lambda=0$, $U_\lambda=U_0$, and for $\lambda=1$, $U_\lambda=U_1$, and such that for any value of $0<\lambda<1$, U_λ is a continuous and differentiable function of λ. For example, a convenient form is

$$U_\lambda = (1-f(\lambda))U_0 + f(\lambda)U \qquad [40]$$

where $f(\lambda)$ is an arbitrary continuous and differentiable function of λ in the interval $0 \leq \lambda \leq 1$, with the property $f(0)=0$ and $f(1)=1$. According to eqn [23], the Helmholtz free energy of this intermediate system is

$$F_\lambda = -k_B T \ln\left\{ \frac{1}{N!\Lambda^{3N}} \int_V d\mathbf{R}_1 \ldots d\mathbf{R}_N e^{-\beta U_\lambda(\mathbf{R}_1, \ldots, \mathbf{R}_N; T)} \right\} \qquad [41]$$

Differentiating this with respect to λ gives

$$\frac{dF_\lambda}{d\lambda} = \frac{\int_V d\mathbf{R}_1 \ldots d\mathbf{R}_N e^{-\beta U\lambda(\mathbf{R}_1, \ldots, \mathbf{R}_N; T)}\left(\frac{\partial U_\lambda}{\partial \lambda}\right)}{\int_V d\mathbf{R}_1 \ldots d\mathbf{R}_N e^{-\beta U_\lambda(\mathbf{R}_1, \ldots, \mathbf{R}_N; T)}} = \left\langle \frac{\partial U_\lambda}{\partial \lambda} \right\rangle_\lambda \qquad [42]$$

and therefore, by integrating $dF_\lambda/d\lambda$, one obtains

$$\Delta F = F_1 - F_0 = \int_0^1 d\lambda \left\langle \frac{\partial U_\lambda}{\partial \lambda} \right\rangle_\lambda \qquad [43]$$

This also represents the reversible work done on the system as the potential energy function is switched from U_0 to U_1.

In most cases, a suitable choice for the function that mixes U_0 and U_1 is simply $f(\lambda) = \lambda$, and the thermodynamic formula [43] takes the simple form

$$\Delta F = F_1 - F_0 = \int_0^1 d\lambda \langle U_1 - U_0 \rangle_\lambda \qquad [44]$$

This way to calculate free energy differences between two systems is called thermodynamic integration (Frenkel and Smit, 1996). The usefulness of the thermodynamic integration formula expressed in eqn [43] becomes clear when one identifies U_1 with the DFT potential (free) energy function and U_0 with some classical model potential for which the free energy is easily calculated, to be taken as a reference system. Then eqn [43] can be used to calculate the DFT free energy of the system by evaluating the integrand $\langle U_1 - U_0 \rangle_\lambda$ using FPMD simulations at a sufficiently large number of values of λ and calculating the integral numerically. Alternatively, one can adopt the dynamic method described by Watanabe and Reinhardt (1990). In this approach, the parameter λ depends on time and is slowly (adiabatically) switched from 0 to 1 during a single simulation. The switching rate has to be slow enough so that the system remains in thermodynamic equilibrium and adiabatically transforms from the reference to the ab initio system. The change in free energy is then given by

$$\Delta F = \int_0^{T_{sim}} dt \frac{d\lambda}{dt} (U_1 - U_0) \qquad [45]$$

where T_{sim} is the total simulation time, $\lambda(t)$ is an arbitrary function of t with the property of being continuous and differentiable for $0 \leq t \leq 1$, $\lambda(0) = 0$, and $\lambda(T_{sim}) = 1$.

Thermodynamic integration can be used to calculate the free energies of both the solids and liquids. It is clear from eqn [43] that the choice of the reference system is almost completely irrelevant (of course, the stability of the system cannot change as λ is switched from 0 to 1), provided that ΔF can be calculated in practice. So, if the goal is to obtain ab initio free energies, it is essential to minimize the amount of ab initio work in order to make the calculations feasible. This is achieved by requiring that (i) the integrand in eqn [43] is a smooth function of λ, (ii) the thermal averages $\langle U_1 - U_0 \rangle_\lambda$ can be computed within the required accuracy on the timescales accessible to FPMD, and (iii) the convergence of ΔF as a function of the number of atoms N in the system is again achieved with N accessible to first-principles calculations. All points (i), (ii), and (iii) could obviously be satisfied by a perfect reference system, that is, a system that differed from the ab initio system only by an arbitrary constant. In this trivial case, the integrand eqn [43] would be a constant, and thermal averages could be calculated on just one configuration and with cells containing an arbitrary small number of atoms. The next thing close to a constant is a slowly varying object, and this therefore provides the recipe for the choice of a good reference system, which has to be constructed in such a way that the fluctuations in $U_1 - U_0$ are as small as possible. If this is the case, thermal averages of $U_1 - U_0$ are readily calculated on short simulations. Moreover, $\langle U_1 - U_0 \rangle_\lambda$ is a smooth function of λ, so a very limited number of simulations for different values of λ are needed and, finally, convergence of $\langle U_1 - U_0 \rangle_\lambda$ with respect to the size of the system is also quick. In fact, if the fluctuations in $U_1 - U_0$ are small enough, one can simply write $F_1 - F_0 \simeq \langle U_1 - U_0 \rangle_0$, with the

average taken in the reference system ensemble. If this is not good enough, the next approximation is readily shown to be

$$F_1 - F_0 \simeq \langle U_1 - U_0 \rangle_0 - \frac{1}{2k_B T} \left\langle \left[U_1 - U_0 - \langle U_1 - U_0 \rangle_0 \right]^2 \right\rangle_0 \qquad [46]$$

This form is particularly convenient since one only needs to sample the phase space with the reference system and perform a number of ab initio calculations on statistically independent configurations extracted from a long classical simulation.

Once the Helmholtz free energy of the system is known, it can be used to derive its thermodynamic properties. For example, it is possible to calculate properties on the so-called Hugoniot line and compare the results with those obtained in shock-wave experiments. The data that emerge most directly from shock-wave experiments consist of a relation between the pressure p_H and the molar volume V_H on the Hugoniot line, which is the set of thermodynamic states given by the Hugoniot–Rankine formula (Poirier, 1991):

$$\frac{1}{2} p_H (V_0 - V_H) = E_H - E_0 \qquad [47]$$

where E_H is the molar internal energy behind the shock front and E_0 and V_0 are the molar internal energy and volume in the zero-pressure state ahead of the front. These experiments are particularly useful in identifying the melting transition. This is done by monitoring the speed of sound, which shows discontinuities at two characteristic pressures p_s and $pl_:$, which are the points where the solid and liquid Hugoniots meet the melting curve. Below p_s, the material behind the shock front is entirely solid, while above p_l, it is entirely liquid; between p_s and p_l, the material is a two-phase mixture. To illustrate an example of the quality of the DFT–GGA predictions of the Hugoniot line, I show in **Figure 7** the calculations of the $p(V)$ relation on the Hugoniot by Alfè et al. (2002a) for solid and liquid iron, compared with the experimental data obtained by Brown and
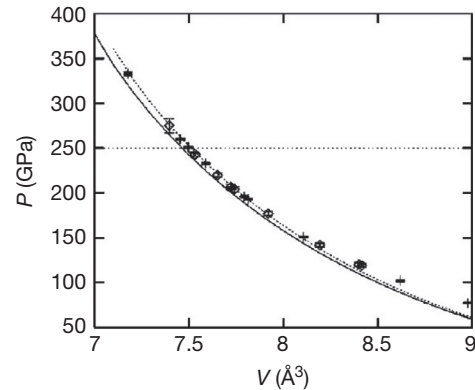
Figure 7 Experimental and first-principles Hugoniot pressure p of Fe as a function of atomic volume V. Symbols show the measurements of Brown and McQueen (1986). Solid curve is first-principles pressure obtained when calculated equilibrium volume of b.c.c. Fe is used in the Hugoniot–Rankine equation; dotted curve is the same, but with experimental equilibrium volume of b.c.c. Fe. The comparison is meaningful only up to a pressure of ca. 250 GPa (horizontal dotted line), at which point the experiments indicate melting. Reprinted from Alfè D, Gillan MJ, and Price GD (2002) *Physical Review B* 65: 165118, with permission. Copyright 2002 American Physical Society.
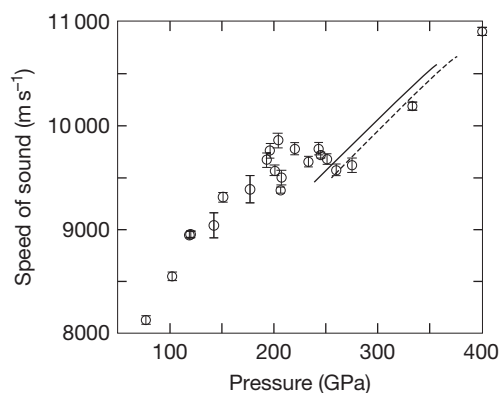
Figure 8 Longitudinal speed of sound on the Hugoniot. Circles, experimental values from Brown and McQueen (1986); continuous and dashed curves, present ab initio values without and with free energy correction (see text). Reprinted from Alfè D, Gillan MJ, and Price GD (2002) *Physical Review B* 65: 165118, with permission. Copyright 2002 American Physical Society.

McQueen (1986). We can see that the agreement between the theory and experiments is extremely good. The two theoretical curves come from raw and free energy-corrected calculations (see the succeeding text). In Figure 8, I show a comparison of the calculated speed of sounds of the liquid with those obtained in the shock-wave experiments. Again, the agreement between the two sets of data is extremely good.

2.15.3.3.4   Melting

The first to use thermodynamic integration in the context of first-principles calculations were Sugino and Car (SC) (1995), who calculated the Gibbs free energies G of solid silicon and liquid silicon at ambient pressure to obtain the DFT–LDA melting temperature T_m, given by the condition $G^l(T_m) = G^s(T_m)$, with superscript l and s indicating the liquid and solid, respectively. In their work, SC used a Stillinger–Weber potential (Stillinger and Weber, 1985) as reference system for both the solid and liquid, coupled with the scheme described in eqn [45] to compute free energy differences. They found that using a switching time T_m of <1 ps was already sufficient to obtain a statistical accuracy on the free energies capable of predicting the melting temperature with an error of the order of 50 K. The importance of the SC work was that it showed that with a judicious choice of the reference system, these kinds of calculations are entirely accessible to first-principles techniques. The calculated LDA melting temperature of Si was 1350 K, about 20% lower than the experimental value (1680 K). Subsequent work showed that by using the GGA approximation, the calculated zero-pressure melting point was ~1500 K (Alfè and Gillan, 2003) and that by using recently developed metaGGA (Staroverov et al., 2004; Tao et al., 2003), the results were very close to the experimental value (Wang et al., unpublished.). Shortly after the work of SC, de Wijs et al. used DFT–LDA in combination with thermodynamic integration to calculate the zero-pressure melting point of Al (de Wijs et al., 1998). They found the value of 890 K, in good agreement with the experimental value 933 K.

Encouraged by these early successes, DFT–GGA and thermodynamic integration were used by Alfè et al. (Alfè, 1999;

Alfè et al., 2001, 2002a) to calculate the free energies of solid and liquid iron under the Earth's core conditions, which they used to obtain a number of thermodynamic properties, including the whole melting curve in the region ~50–400 K. They discovered that a simple sum of inverse power pair potentials of the form $U_{IP}(r) = B/r^\alpha$, where r is the distance between two ions and B and α are two adjustable parameters, did an excellent job in describing the energetics of the liquid and the high-temperature solid, provided that B and α were appropriately adjusted. As mentioned in the previous section, an additional crucial advantage of having a good reference system is that convergence of $F_1 - F_0$ with respect to the size of the system is very rapid, and in fact, for both solid iron and liquid iron, Alfè et al. found that already with 64-atom systems, $F_1 - F_0$ was converged to within better than 10 meV per atom, which in turn implied melting temperature converged to better than 100 K with respect to this single technical point. Their best estimate for the melting point at the inner–outer core boundary pressure of 330 GPa was $T_m = 6350 \pm 300$ K, where the error quoted is the result of the combined statistical errors in the free energies of the solid and liquid. Systematic errors due to the approximations of DFT are more difficult to estimate, and additional information can only be obtained when the problem is studied using a more accurate implementation of quantum mechanics. I will come back to this point later in the chapter.

At the present state of knowledge, the experimental understanding of the melting point of Fe under the Earth's core conditions is still scarce, as experiments based on diamond-anvil cells (DAC) cannot reach these pressures. Moreover, even in the region of the phase space where DAC experiments are possible, there is still considerable disagreement between different groups (Boehler, 1993; Ma et al., 2004; Shen et al., 1998) and between DAC and shock-wave experiments (Brown and McQueen, 1986; Nguyen and Holmes, 2004). However, the state of the art is improving, and very recently, two new DAC experiments have highlighted the difficulty of detecting the melting transition in older experiments (Boehler, 1993). Jackson et al. (2013) used synchrotron Mössbauer spectroscopy to monitor the dynamics of the iron atoms, and Anzellini et al. (2013) used x-ray spectroscopy to identify the onset on melting from the complete disappearance of peaks due to the presence of the solid from the spectrum. In particular, Anzellini et al. (2013) found that before melting, the system goes through a fast recrystallization process, at a temperature very close to that measured by Boehler (1993). They therefore suggested that this was the process detected in these older experiments (Boehler, 1993) and not melting. The results of Anzellini et al. (2013) agree very closely with the theoretical predictions of Alfè et al. (2002a).

On the theoretical side, I mention also the work of Laio et al. (2000) and Belonoshko et al. (2000), who performed DFT-based simulations to calculate the melting curve of Fe under the Earth's core conditions, although their approach was rather different from that of Alfè (1999) and Alfè et al. (2001, 2002a). Instead of calculating free energies, Laio et al. (2000) and Belonoshko et al. (2000) fitted a classical model potential to their first-principles calculations and then used the classical potential to compute the melting curve. To do so, they used the coexistence method, in which the solid and liquid are

simulated in contact in a box. This method is an alternative route to the calculation of melting curves and therefore equivalent to the free energy approach. However, Laio et al. and Belonoshko et al. found that at the pressure of 330 GPa, iron melted at 5400 and 7000 K, respectively. The reason of these large differences and the difference with the value 6350 K reported by Alfè et al. is due to the quality of the classical potentials employed and in particular to the free energy differences between these classical potentials and the DFT system. This was later investigated by Alfè et al. (2002b), who showed that it is possible to assess the differences in free energies between the classical potential and the DFT one and correct for it. In particular, it was shown that at a fixed pressure p, the first approximation of the difference T' in the melting temperature between the classical potential and the ab initio system is given by

$$T' = \Delta G^{ls}(T_{mod})/S^{ls}_{mod} \qquad [48]$$

where S^{ls}_{mod} is the entropy of fusion of the model potential, T_{mod} its melting temperature, and $\Delta G^{ls} = (G^l_{ab} - G^l_{mod}) - (G^s_{ab} - G^s_{mod})$, where G is the Gibbs free energy; the subscripts 'ab' and 'mod' indicate the ab initio and the model system, respectively; and the superscripts 'l' and 's' indicate the liquid and solid, respectively. These differences of Gibbs free energies can be calculated using thermodynamic integration, which if the model potential is not too different from the ab initio, one can be calculated using the perturbative approach outlined in eqn [46] in the preceding text. The relation between ΔG, evaluated at constant p, and ΔF, calculated at constant V, is readily shown to be

$$\Delta G = \Delta F - \frac{1}{2}V\kappa_T\Delta p^2 + o(\Delta p^3) \qquad [49]$$

where κ_T is the isothermal compressibility and Δp is the change of pressure when U_{mod} is replaced by U_{ab} at constants V and T. Once these corrections were applied, the results of Belonoshko et al. (2000) came in perfect agreement with those of Alfè et al. (2002a). These results are all displayed in Figure 9, together with a number of experimental data.

The coexistence method mentioned in the preceding text is an alternative route to the calculation of melting properties and as such delivers the same results if applied consistently. For its very nature, the method is intrinsically very expensive, because it requires simulations on systems containing a large number of atoms, typically many hundreds or even thousands. For this reason, until very recently, it had been only applied to calculations employing classical potentials. However, it has been recently shown that the method can in fact be applied also in the context of first-principles calculations. As computers become faster and faster, this method will become more and more common also within the context of first-principles calculations.

In Figure 10, I show the low-pressure melting curve of aluminum, as obtained by Vočadlo and Alfè with the free energy approach and the GGA XC potential (Vočadlo and Alfè, 2002) and, later, with the coexistence approach (Alfè, 2003), using the very same electronic structure techniques. This was the first time that the coexistence method was being applied using first-principles techniques. The simulations were performed on systems containing up to 1728 atoms, and the results showed that already, with modest system sizes of 512 atoms, the points calculated with the coexistence approach
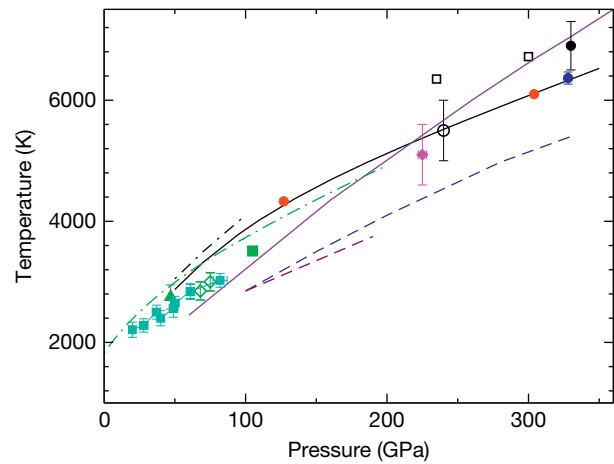

Figure 9 Comparison of melting curve of Fe from DFT calculations and experimental data. Black solid curve, first-principles results of Alfè et al. (2002a); blue-filled circle, first-principles coexistence result from Alfè (2009b); red-filled circles, corrected coexistence results from Alfè et al. (2004); black-filled circle, QMC result from Sola and Alfè (2009); blue dashed curve, empirical potential results of Laio et al. (2000); purple curve, empirical potential results of Belonoshko et al. (2000); black chained and maroon dashed curves, DAC measurements of Williams et al. (1987) and Boehler (1993); green diamonds and green-filled square, DAC measurements of Shen et al. (1998) and Ma et al. (2004); magenta-filled squares, DAC measurements of Jackson et al. (2013); green chained curve: DAC measurements of Anzellini et al. (2013); black open squares, black open circle, and magenta diamond: shock-wave experiments of Yoo et al. (1993), Brown and McQueen (1986), and Nguyen and Holmes (2004). Error bars are those quoted in original references.
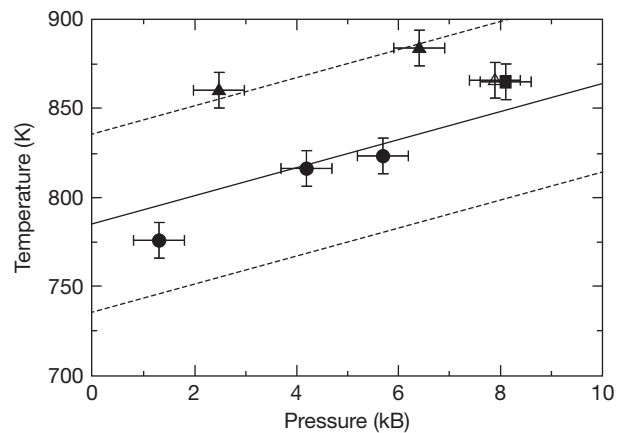

Figure 10 Temperatures and pressures at which liquid and solid Al coexist in first-principles simulations containing 1728 atoms (filled square), 1000 atoms (filled circles), and 512 atoms (filled triangles) performed using Γ-point sampling only. Open triangle is the result from a $2 \times 2 \times 1$ **k**-point grid on a 512-atom system. The solid line is the lower end of the melting curve calculated using the free energy approach in Vočadlo and Alfè (2002) (see text); light dashed lines represent error bars. Results from simulations using Γ-point sampling only for 1000- and 512-atom systems were reported in Alfè (2003).

differed from those obtained with the free energy approach by no more than 50 K. In fact, this difference was reduced even further if the 512-atom simulation was carried out with a denser **k**-point grid sampling, showing that genuine size effects

are very small already in systems containing 512 atoms. Note that the zero-pressure melting temperature of 786 K obtained with the GGA is not in very good agreement with the experimental value 933 K. It was argued (Vočadlo and Alfè, 2002) that the main cause of this discrepancy was a deficiency of the GGA of predicting the correct zero-pressure density, which comes out to be too large, and this would effectively correspond to calculating the melting temperature at a negative pressure. By applying a correction to the Helmholtz free energy in order to obtain the zero-pressure density for the solid and assuming that the same correction also applied to the liquid, they found that this corrected free energy predicted a zero-pressure melting temperature of 912 K, in excellent agreement with the experimental datum.

A short time after the coexistence work on aluminum, a second calculation using the same technique to calculate the melting curve of LiH appeared (Ogitsu et al., 2003) and more recently for the calculation of the melting curve of hydrogen up to 200 GPa (Bonev et al., 2004) and the melting curve of MgO in the pressure range 0–135 GPa (Alfè, 2005), reported in Figure 11. This last work was performed with both the LDA and the GGA exchange-correlation functionals, and despite that the results at high pressure were very similar, at zero pressure, the two calculations differed by about 20%, with the LDA being in good agreement with the experimental datum and the GGA predicting a lower melting temperature. This work also pointed out that the contribution of the electronic entropy to the free energy was nonnegligible and very different between the solid and liquid, such that it is responsible of a lowering of about 130(750) K of the melting temperature in the low(high)-pressure region of the phase diagram. This may be surprising, as solid MgO is a large band gap insulator, and indeed, a significant band gap remains in the high-temperature solid. However, the absence of local order in the liquid is such that the band gap is greatly reduced, with a correspondingly significant increase of electronic entropy. In fact, recent experiments find that above 600 GPa, the electrical conductivity of liquid MgO increases significantly, suggesting that under these conditions, it becomes a metal (McWilliams et al., 2012). This emphasizes the need to accurately include electronic effects in the calculation of melting properties.

I now return to the melting point of iron at ICB pressures to describe two recent developments on the simulation side. Taking advantage of the large increase in computer power, I revisited the problem by performing a series of coexistence simulations using cells containing 980 atoms, using DFT. The simulations were performed at fixed cell lattice parameters, which results in slight nonhydrostatic conditions. To estimate both the effect of nonhydrostaticity and finite simulation cell size, I performed constant-stress simulation on much larger systems (7840 atoms) using an embedded atom model constructed to closely reproduce the energetics of iron at these conditions. The tests showed that nonhydrostaticity is responsible for an underestimate of the melting temperature by $\simeq 100$ K and finite size for an overestimate of $\simeq 100$ K, so that the two errors cancel each other. The simulation provided a melting point of 6370 ± 100 K at 328 GPa, which is on the melting curve obtained using the free energy approach (Alfè et al., 2002a). Around the same time, Sola and Alfè (2009) used QMC methods to investigate the accuracy of DFT at predicting the melting point of iron at the Earth's core conditions. This was done by computing free energy differences between QMC and DFT using the perturbative method described in eqns [46] and [48] in the preceding text. The calculations showed a slight increase of melting temperature to 6900 ± 400 K (the error corresponds to one standard deviation), which essentially confirmed the DFT prediction of a 'high' melting point of iron at the Earth's core conditions.
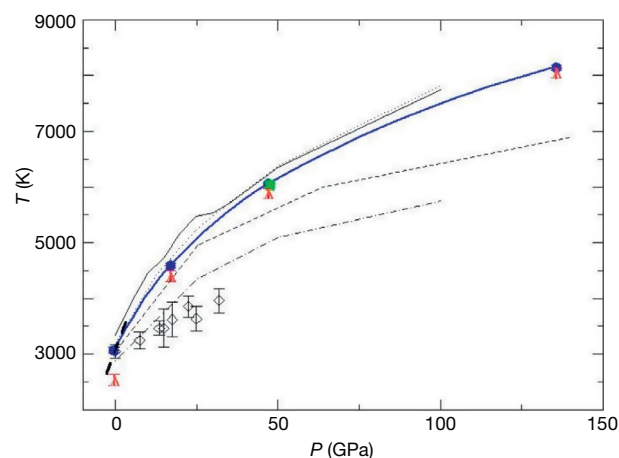
2.15.3.3.5   Solutions

I now turn the discussion to systems formed by more than one species of atoms. For example, consider two different substances and mix them together, and in general, they will form a solution, like sugar and coffee. I call solvent the substance present in the largest quantity (coffee) and solute the other (sugar). In general, solutions may have more than one solute and/or more than one solvent, but for simplicity, we will focus here only on binary mixtures.

In this section, I want to discuss how first-principles methods can be used to study the thermodynamic properties of solutions. As an example of the methods to be discussed, I will present calculations on iron alloyed with either sulfur or silicon or oxygen, at the conditions of pressure and temperature of the Earth's inner-core boundary, and how these calculations have been used to estimate the composition of the core. The techniques, however, are completely general and can be applied also to other systems under different thermodynamic conditions.

As mentioned in the preceding text, the behavior of solutions can be understood in terms of the chemical potential μ_i, defined in eqns [30] and [31]. Consider now a solution with N_A particles of solvent A and N_X particles of solute X, with $N = N_A + N_X$. In the high temperature limit, the Helmholtz free energy of this system is

Figure 11   Melting curve of MgO obtained with DFT–LDA coexistence simulations performed on 432-atom cells (blue dots and heavy solid line), 1024-atom cell (green square), and DFT–GGA results (red triangles; Alfè, 2005), compared with experiments (open diamonds; Zerr and Boehler, 1994). Other curves show results of earlier modeling work based on interaction models. Reproduced from Alfè D (2005) *Physical Review Letters* 94: 235701, with permission. Copyright 2005 American Physical Society.

$$F = -k_B T \ln \frac{1}{\Lambda_A^{3N_A} \Lambda_X^{3N_X} N_A! N_X!} \int_V d\mathbf{R}_1 \dots d\mathbf{R}_N e^{-U(\mathbf{R}_1, \dots, \mathbf{R}_N; T)/k_B T}$$

[50]

According to eqn [31], we have

$$\mu_X = \left(\frac{\partial F}{\partial N_X}\right)_{T,V} = F(N_A, N_X + 1) - F(N_A, N_X)$$ [51]

which can be evaluated using eqn [50]:

$$\mu_X = -k_B T \ln \frac{1}{\Lambda_X^3 (N_X + 1)}$$

$$\frac{\int_V d\mathbf{R}_1 \dots d\mathbf{R}_N d\mathbf{R}_{N+1} e^{-U(\mathbf{R}_1, \dots, \mathbf{R}_N, \mathbf{R}_{N+1}; T)/k_B T}}{\int_V d\mathbf{R}_1 \dots d\mathbf{R}_N e^{-U(\mathbf{R}_1, \dots, \mathbf{R}_N; T)/k_B T}}$$

[52]

The ratio of the two integrals is an extensive quantity, but μ_X is an intensive quantity; therefore, it is useful to rewrite the expression as follows:

$$\mu_X = -k_B T \ln \frac{N}{(N_X + 1)}$$

$$\left\{ \frac{1}{N \Lambda_X^3} \frac{\int_V d\mathbf{R}_1 \dots d\mathbf{R}_N d\mathbf{R}_{N+1} e^{-U(\mathbf{R}_1, \dots, \mathbf{R}_N, \mathbf{R}_{N+1}; T)/k_B T}}{\int_V d\mathbf{R}_1 \dots d\mathbf{R}_N e^{-U(\mathbf{R}_1, \dots, \mathbf{R}_N; T)/k_B T}} \right\}$$

[53]

so that the value in curly brackets is now independent on system size. By setting $c_X = N_X/N$ (which in the limit of large N and N_X is the same as $(N_X + 1)/N$) and

$$\tilde{\mu}_X = -k_B T \ln \left\{ \frac{1}{N \Lambda_X^3} \frac{\int_V d\mathbf{R}_1 \dots d\mathbf{R}_N d\mathbf{R}_{N+1} e^{-U(\mathbf{R}_1, \dots, \mathbf{R}_N, \mathbf{R}_{N+1}; T)/k_B T}}{\int_V d\mathbf{R}_1 \dots d\mathbf{R}_N e^{-U(\mathbf{R}_1, \dots, \mathbf{R}_N; T)/k_B T}} \right\}$$

[54]

we can rewrite the chemical potential in our final expression:

$$\mu_X(p, T, c_X) = k_B T \ln c_X + \tilde{\mu}_X(p, T, c_X)$$ [55]

The first term of eqn [55] depends only on the number of particles of solute present in the solution, while the second term is also responsible for all possible chemical interactions.

For small concentration of solute, we can make a Taylor expansion of $\tilde{\mu}_X$:

$$\tilde{\mu}_X = \mu_X^0 + \lambda c_X + o(c_X^2)$$ [56]

where $\lambda = (\partial \tilde{\mu}_X / \partial c_X)_{p,T}$. If the solution is so dilute that the particles of the solute do not interact with each other, we can stop the expansion to the first term, and we have

$$\mu_X(p, T, c_X) = k_B T \ln c_X + \mu_X^0(p, T)$$ [57]

A system in which eqn [57] is strictly satisfied is called an ideal solution.

To find an expression for the chemical potential of the solvent, we employ the Gibbs–Duhem equation, which for a system at constant pressure and constant temperature reads (Wannier, 1966)

$$\sum_i N_i d\mu_i = 0$$ [58]

In particular, in our two-component system, the Gibbs–Duhem equation implies

$$c_A d\mu_A + c_X d\mu_X = 0$$ [59]

which gives (Alfè et al., 2002c)

$$\mu_A(p, T, c_X) = \mu_A^0(p, T) + (k_B T + \lambda_X(p, T)) \ln (1 - c_X)$$
$$+ \lambda_X(p, T) c_X + O(c_X^2)$$ [60]

where μ_A^0 is the chemical potential of the pure solvent. To linear order in c_X, this gives

$$\mu_A(p, T, c_X) = \mu_A^0(p, T) - k_B T c_X + O(c_X^2)$$ [61]

Despite that μ_A^0 is the chemical potential of the pure solvent, note that μ_X^0 is not the chemical potential of the pure solute, unless the validity of eqn [57] extends all the way up to $c_X = 1$.

2.15.3.3.6 First-principles calculations of chemical potentials

To calculate μ_X, it is useful to consider the difference in chemical potential between the solute and the solvent $\mu_{XA} = \mu_X - \mu_A$, which is equal to the change of Helmholtz free energy of the system as one atom of the solvent is transmuted into an atom of solute at constant volume V and constant temperature p. This transmutation does not obviously correspond to a real physical process, but provides a perfectly rigorous way of calculating the difference of chemical potentials:

$$\mu_{XA} = k_B T \ln \frac{c_X}{1 - c_X} + 3k_B T \ln (\Lambda_X / \Lambda_A) + m(c_X)$$ [62]

where Λ_X and Λ_A are the thermal wavelengths of solute and solvent and

$$m(c_X) = -k_B T \ln \frac{\int_V d\mathbf{R} e^{-\beta U(N_A - 1, N_X + 1; \mathbf{R})}}{\int_V d\mathbf{R} e^{-\beta U(N_A, N_X; \mathbf{R})}}$$ [63]

with $U(N_A, N_X; \mathbf{R})$ being the potential energy of the system with N_A atoms of solvent and N_X atoms of solute and $u(N_A - 1, N_X + 1; \mathbf{R})$ being the one for the system in which one of the atoms of solvent has been transmuted into the solute.

The thermodynamic integration technique described in Section 2.15.3.3.3 can now be used to compute $m(c_X)$ in the liquid state. This is done by defining an intermediate potential $U_\lambda = \lambda U(N_A - 1, N_X + 1; \mathbf{R}) + (1 - \lambda)U(N_A, N_X; \mathbf{R})$, so that $m(c_X)$ can be expressed as

$$m(c_X) = \int_0^1 d\lambda \langle U(N_A - 1, N_X + 1) - U(N_A, N_X)\rangle_\lambda$$ [64]

In practice, the calculation of $m(c_X)$ is done by performing two separate simulations, one with N_A atoms of solvent and N_X of solute and the other with $N_A - 1$ atoms of solvent and $N_X + 1$ atoms of solute. At the end of each time step, forces are computed in both systems, and their linear combination $f_\lambda = \lambda f(N_A - 1, N_X + 1) + (1 - \lambda) f(N_A, N_X)$ is used to evolve the system in time in order to compute the thermal average $\langle U(N_A - 1, N_X + 1) - U(N_A, N_X)\rangle_\lambda$. This is repeated at a number of different values of λ, and the integral is performed numerically. Alternatively, an approach similar to the one described in

eqn [45] is also possible, in which λ is slowly varied from zero to one in the course of the simulation.

To improve statistics, it is useful to transmute many atoms of solvent into solute. In this case, one does not obtain directly μ_{XA} at a chosen concentration, but an integral of this over a range of concentrations. However, by repeating the calculations transmuting a different number of atoms at a time, it is possible to extract information about the value of μ_{XA} in a whole range of concentration, as described in Alfè et al. (2002c). To illustrate the feasibility of these kinds of calculations, in Figure 12, we show the value of the integrand in eqn [64] as function of lambda for an iron–oxygen liquid mixture at a pressure of 370 GPa and a temperature of 7000 K. The error in calculating this integral is of the order of 0.1 eV, which is very small for the purposes of evaluating the partitioning of oxygen between solid iron and liquid iron and the depression of melting point resulting from this partitioning (see the succeeding text). This pressure is somewhat higher than the ICB pressure of 330 GPa. The temperature is also higher than the melting temperature of iron; however, it was argued in Alfè et al. (2002c) that this would not change the chemical potential of O by more than 0.3 eV, which again does not have any effect of the conclusions to be presented in the succeeding text.

In the solid state, thermodynamic integration is not the most appropriate way of calculating the chemical potential difference μ_{XA}. This is clear, because in the zero-temperature limit, at infinite dilution, $m(c_X \rightarrow 0)$ is simply the change in internal energy when one atom in the perfect lattice of solvent is replaced by a solute atom, the impurity system being relaxed to equilibrium. This requires only a static calculation of the type described in Section 2.15.3.1. At finite temperatures in the infinite dilution limit, $m(c_X \rightarrow 0)$ can be obtained from the quasi-harmonic vibrational frequencies of the pure A system and the system containing a single X impurity. If anharmonic effects are significant, as they are in the case of O substituted in hcp Fe (Alfè et al., 2000b), thermodynamic integration can be used to estimate the anharmonic effects. These methods can also be generalized to include the variation of $m(c_X)$ with c_X to linear order in c_X (Alfè et al., 2002c).

The evaluation of $m(c_X)$ only gives access to the difference between the chemical potential of the solute and that of the solvent. Therefore, in order to obtain μ_X, a preliminary calculation of μ_A is necessary. This can be done on the pure solvent system using the techniques described in Section 2.15.3.3.3.

2.15.3.3.7 Volume of mixing

It is often interesting to study the change of volume of a solution as a function of the concentration of solute. To this end, it is useful to express the volume of the system as the partial derivative of the Gibbs free energy with respect to pressure, taken at constant temperature and number of particles:

$$V = (\partial G / \partial p)_{T, N_X, N_A} \qquad [65]$$

If we now add to the system one particle of solvent at constant pressure, the total volume changes by v_A and becomes $V + v_A$. We call v_A the partial molar volume of the solvent. The total Gibbs free energy is $G + \mu_A$, so that according to eqn [65], $v_A = (\partial \mu_A / \partial p)_{T, N_X, N_A} = (\partial \mu_A / \partial p)_{T, c_X}$ where the last equality stems from the fact that μ_A only depends on N_X and N_A through the molar fraction c_X (we assume here that c_X does not change when we add one particle of solvent to the system; this is obviously true if the number of atoms of solvent N_A is already very large.). The partial volume in general depends on c_X, p, and T, but under the assumption of ideality, $v_A = (\partial \mu_A^0 / \partial p)_{T, c_X}$, and it depends only on p and T. In an ideal solution, v_A is the same as in the pure solvent.

Similarly, the partial molar volume of the solute is $v_X = (\partial \mu_X / \partial p)_{T, c_X}$, which becomes independent on c_X under the assumption of ideality. Notice that this is not in general equal to the partial volume of the pure solute.

As an example of the calculation of partial molar volumes, we mention the partial molar volumes of iron and X, with X being either sulfur or silicon or oxygen, obtained by Alfè et al. (2002d) in a binary mixture of iron at the conditions mentioned above of $p = 370$ GPa and $T = 7000$ K. These were $v_{Fe} = 6.97$ Å^3, $v_{Si} = 6.65$ Å^3, $v_S = 6.65$ Å^3, and $v_O = 4.25$ Å^3. Although ideality was not assumed in these calculations, the partial molar volumes of Si, S, and O were found to be rather independent from their concentration in liquid Fe. It is interesting to note that both sulfur and silicon have a partial molar volume that is very similar to that of iron, while oxygen is significantly smaller. This is the main reason of the large difference in the behavior of sulfur and silicon on the one side and oxygen on the other and the resulting partitioning of oxygen between solid and liquid iron (see the succeeding text).

2.15.3.3.8 Solid liquid equilibrium

We want to study now the conditions that determine equilibrium between solid and liquid and in particular how the solute partitions between the two phases and how this partitioning affects the melting properties of the solution. Thermodynamic equilibrium is reached when the Gibbs free energy of the system is at its minimum, and therefore, $0 = dG = d(G^l + G^s)$, where superscripts 's' and 'l' indicate quantities in the solid and the liquid, respectively. In a multicomponent system, the Gibbs free energy can be expressed in terms of the chemical potentials of the species present in the system (Mandl, 1997; Wannier, 1966):
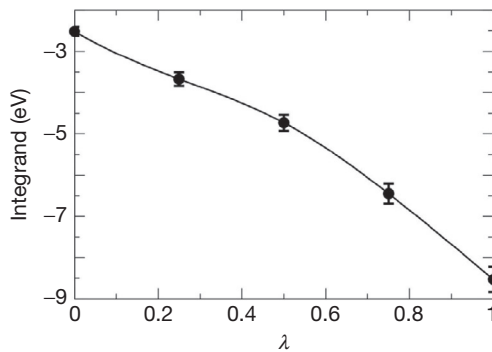

Figure 12 The integrand $\langle U_1 - U_0 \rangle_\lambda$ (eV units) appearing in the thermodynamic integration formula in eqn [64]. Results shown refer to oxygen solute for $N_X = 12$ and $N = 64$. Filled circles show values computed from ab initio m.d. simulations, with bars indicating statistical errors. Curve is a polynomial fit to the computed values.

$$G = \sum_i N_i \mu_i \qquad [66]$$

Using eqn [66] and the Gibbs–Duhem equation [58], we obtain

$$dG = \sum_i \mu_i dN_i \qquad [67]$$

If the system is isolated, particles can only flow between the solid and the liquid, and we have $dN_i^s = -dN_i^l$, which implies

$$dG = \sum_i dN_i (\mu_i^l - \mu_i^s) \qquad [68]$$

If $\mu_i^l < \mu_i^s$, there will be a flow of particles from the solid to the liquid region ($dN_i > 0$), so that the Gibbs free energy of the system is lowered. The opposite will happen if $\mu_i^l > \mu_i^s$. The flow stops at equilibrium, which is therefore reached when $\mu_i^l = \mu_i^s$. In particular, in our two components system, equilibrium between the solid and liquid implies that the chemical potentials of both the solvent and solute are equal in the solid and liquid phases:

$$\mu_X^s(p, T_m, c_X^s) = \mu_X^l(p, T_m, c_X^l)$$
$$\mu_X^s(p, T_m, c_X^s) = \mu_A^l(p, T_m, c_X^l) \qquad [69]$$

where T_m is the melting temperature of the solution at pressure p. Using eqn [55], we can rewrite the first of the two equations in the preceding text as

$$\tilde{\mu}_X^s(p, T_m) + k_B T_m \ln c_X^s = \tilde{\mu}_X^l(p, T_m) + k_B T_m \ln c_X^l \qquad [70]$$

From which, we obtain an expression for the ratio of concentrations of solute between the solid and the liquid:

$$c_X^s / c_X^l = \exp\left\{ \left[\tilde{\mu}_X^l(p, T_m) - \tilde{\mu}_X^s(p, T_m) \right] / k_B T_m \right\} \qquad [71]$$

In general, $\tilde{\mu}_X^l < \tilde{\mu}_X^s$, because the greater mobility of the liquid can usually better accommodate particles of solute, and therefore, their energy (chemical potential) is lower. This means that the concentration of the solute is usually smaller in the solid.

Equation [71] was used by Alfè et al. (2000c, 2002c,d) to put constraints on the composition of the Earth's core. The constraints came from a comparison of the calculated density contrast at inner-core boundary and that obtained from seismology, which is between $4.5 \pm 0.5\%$ (Masters and Shearer, 1990) and $6.7 \pm 1.5\%$ (Masters and Gubbins, 2003). This density contrast is significantly higher than that due to the crystallization of pure iron and therefore must be due to the partitioning of light elements between the solid and liquid. Alfè et al. (2000c, 2002c,d) considered sulfur, silicon, and oxygen as possible impurities and using first principles obtained the partitions for each impurity. The calculations showed that for both sulfur and silicon, $\tilde{\mu}_X^l$ and $\tilde{\mu}_X^s$ are very similar, which means that c_X^s and c_X^l are also very similar, according to eqn [71]. As a result, the density contrast of a Fe/S or a Fe/Si system is not much different from that of pure Fe and still too low when compared with the seismological data. By contrast, for oxygen, $\tilde{\mu}_o^l$ and $\tilde{\mu}_o^s$ are very different, and the partitioning between the solid and liquid is very large. This results in a much too large density contrast, which also does not agree with the seismological data. These results are
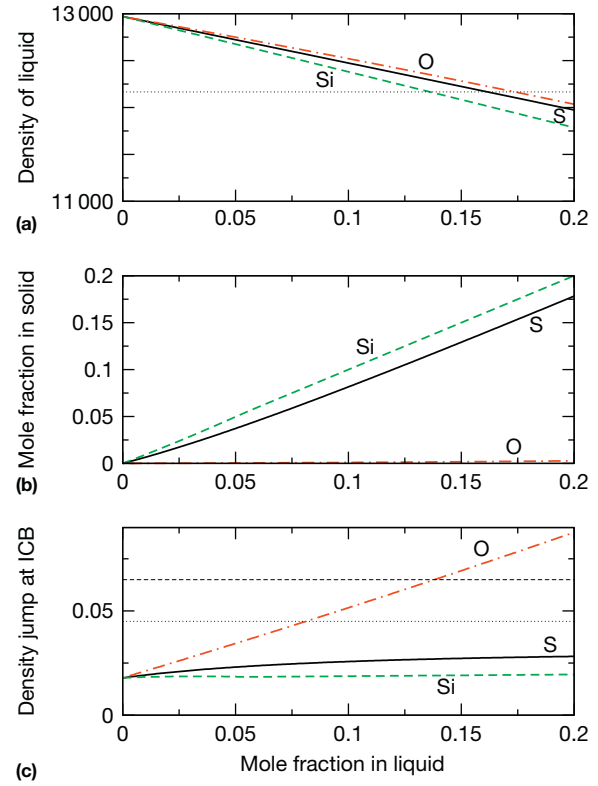

Figure 13 Liquid and solid impurity mole fractions c_X^l and c_X^s of impurities X = S, Si, and O and resulting densities of the inner and outer core of the Earth predicted by first-principles simulations. Solid, dashed, and chain curves represent S, Si, and O, respectively. (a) Liquid density ρ^l (kg m^{-3} units); horizontal dotted line shows density from seismic data (Dziewonski and Anderson, 1981; Masters and Shearer, 1990); (b) mole fractions in solid resulting from equality of chemical potentials in the solid and liquid; (c) relative density discontinuity $\delta\rho/\rho^l$ at the ICB; horizontal dotted and dashed lines are values from free oscillation data (Masters and Gubbins, 2003; Masters and Shearer, 1990). Adapted from Alfè D, Gillan MJ, and Price GD (2002) *Earth and Planetary Science Letters* 195: 91, with permission. Copyright 2002 Elsevier.

summarized in Figure 13. The conclusion from these calculations was that none of these binary mixtures can be viable for the core. The density contrast can of course be explained by ternary or quaternary mixtures. Assuming no cross correlated effects between the chemical potentials of different impurities and based on the seismological density contrast of $4.5 \pm 0.5\%$ (Masters and Shearer, 1990), Alfè et al. (2002c,d) proposed an inner core containing about 8.5% of sulfur and/or silicon and almost no oxygen and an outer core containing about 10% of sulfur and/or Si and an additional 8% of oxygen. The more recent seismological datum of $6.7 \pm 1.5\%$ (Masters and Gubbins, 2003) would change the estimate of the core composition to an inner core containing about 7% of sulfur and/or silicon and still almost no oxygen and an outer core containing about 8% of sulfur and/or Si and an additional 13% of oxygen. One consequence of the large partitioning of oxygen between the solid and liquid is that as the solid core grows, it expels oxygen in the liquid, which by converting its gravitational energy helps driving the convective motions that are

responsible for the generation of the Earth's magnetic field (Gubbins et al., 2004).

2.15.3.3.9 Shift of freezing point

The partitioning of the solute between the solid and the liquid is generally responsible for a change in the melting temperature of the mixture with respect to that of the pure solvent. To evaluate this, we expand the chemical potential of the solvent around the melting temperature of the pure system, T_m^0:

$$\mu_A(p, T_\mathrm{m}, c_X) = \mu_A\left(p, T_\mathrm{m}^0, c_X\right) - s_A^0 \delta T + \dots \qquad [72]$$

where $\delta T = \left(T_\mathrm{m} - T_\mathrm{m}^0\right)$ and $s_A^0 = -(\partial \mu_A / \partial T)_{T = T_\mathrm{m}^0}$ are the entropy of the pure solvent at T_m^0. We now impose continuity across the solid/liquid boundary:

$$\mu_A^{0s}\left(p, T_\mathrm{m}^0\right) - s_A^{0s} \delta T - k_B T_\mathrm{m} c_X^s = \mu_A^{0l}\left(p, T_\mathrm{m}^0\right) - s_A^{0l} \delta T - k_B T_\mathrm{m} c_X^l \qquad [73]$$

where we have considered only the linear dependence of μ_A on c_X (see eqn [61]). Noting that $\mu_A^{0s}(p, T_\mathrm{m}^0) = \mu_A^{0l}(p, T_\mathrm{m}^0)$, we have

$$\delta T = \frac{kT_\mathrm{m}}{s_A^{0l} - s_A^{0s}}\left(c_X^s - c_X^l\right) \qquad [74]$$

Since usually $c_X^s < c_X^l$, there is generally a depression of the freezing point of the solution.

Using eqn [74] and the composition estimated from the density contrast of 4.5%, Alfè et al. (2002c,d) estimated a depression of about 600–700 K of the melting temperature of the core mixture with respect to the melting temperature of pure Fe, and they suggested an inner-core boundary temperature of about 5700 K. This estimate would go down by a further 300 K if the latest estimate of 6.7% for the density contrast at ICB was used (Masters and Gubbins, 2003), which would therefore result in a temperature at the ICB of about 5500 K.

2.15.3.3.10 Electrical and thermal conductivity

Electrical and thermal conductivities of materials can be calculated from first principles. In particular, in the context of DFT, the frequency-dependent electrical conductivity can be calculated by using the Kubo–Greenwood formula (Kubo, 1957; Greenwod, 1958), which for a particular $\mathbf{k}$-point in the BZ of the simulation supercell and for a particular configuration of the ions $\{R_I\}$ reads

$$\sigma_\mathbf{k}(\omega; R_I) = \frac{2\pi e^2 \hbar^2}{3m^2\omega\Omega} \sum_{i,j=1}^{n} \sum_{\alpha=1}^{3} \left[F(\varepsilon_{i,\mathbf{k}}) - F(\varepsilon_{j,\mathbf{k}})\right] |\langle \Psi_{j,\mathbf{k}}|\nabla_\alpha|\Psi_{i,\mathbf{k}}\rangle|^2 \delta$$
$$\left(\varepsilon_{j,\mathbf{k}} - \varepsilon_{i,\mathbf{k}} - \hbar\omega\right) \qquad [75]$$

where ω is the angular frequency; e and m are the electron charge and mass, respectively; $\hbar$ is the Plank's constant divided by 2π; Ω is the volume of the simulation cell; and n is the number of Kohn–Sham states. The α sum runs over the three spatial directions. $\Psi_{i,\mathbf{k}}$ is the Kohn–Sham wave function corresponding to eigenvalue $\varepsilon_{i,\mathbf{k}}$, and $F(\varepsilon_{i,\mathbf{k}})$ is the Fermi weight. The δ function is represented by a Gaussian, with a width chosen to be roughly equal to the average spacing between the eigenvalues weighted by the corresponding change in the Fermi function (Desjarlais et al., 2002). In a liquid or in a solid above zero temperature, the frequency-dependent conductivity is obtained by taking the thermal average:

$$\sigma(\omega) = \left\langle \sum_\mathbf{k} \sigma_\mathbf{k}(\omega; R_I) W(\mathbf{k}) \right\rangle \qquad [76]$$

where $W(\mathbf{k})$ is the weighting factor for the point $\mathbf{k}$. The dc conductivity σ_0 is given by the value of $\sigma(\omega)$ in the limit $\omega \to 0$.

In a free electron liquid, the electronic part of the thermal conductivity κ_0 and the electrical conductivity σ_0 are related by the Wiedemann–Franz law (Wiedemann and Franz, 1853), $L = \kappa_0/\sigma_0 T$, where L is the Lorenz number. In a real liquid, the validity of the Wiedemann–Franz law is not necessarily expected, and in fact, a number of exceptions for metals at near-ambient conditions are known (see, e.g., Kittel, 1996). However, the electronic component of the thermal conductivity κ_0 can be directly calculated using the Chester and Thellung (1961) formulation of the Kubo–Greenwood formula, which reads

$$\kappa(\omega) = \frac{1}{e^2 T}\left(L_{22}(\omega) - \frac{L_{12}(\omega)^2}{\sigma(\omega)}\right) \qquad [77]$$

and κ_0 is the value of $\kappa(\omega)$ in the limit $\omega \to 0$. The kinetic coefficients $L_{lm}(\omega)$ are given by Mazevet et al. (2010)

$$L_{lm}(\omega) = (-1)^{(l+m)} \frac{2\pi e^2 \hbar^2}{3m^2\omega\Omega} \sum_{i,j=1}^{n} \sum_{\alpha=1}^{3} \left[F(\varepsilon_{i,\mathbf{k}}) - F(\varepsilon_{j,\mathbf{k}})\right] |\langle \Psi_{j,\mathbf{k}}|\nabla_\alpha|\Psi_{i,\mathbf{k}}\rangle|^2$$
$$\times \left[\varepsilon_{j,\mathbf{k}} - \mu\right]^{(l-1)}\left[\varepsilon_{i,\mathbf{k}} - \mu\right]^{(m-1)} \delta\left(\varepsilon_{j,\mathbf{k}} - \varepsilon_{i,\mathbf{k}} - \hbar\omega\right) \qquad [78]$$

where μ is the chemical potential.

As an example of a recent application, I mention the first-principles calculation of electrical and thermal conductivities of iron and iron alloys (Pozzo et al., 2012, 2013) under the Earth's core conditions, which are displayed in **Figure 14**. The conductivities have been calculated on three possible adiabatic pressure–temperature profiles, anchored at the ICB temperatures of 6350, 5700, and 5500 K, corresponding to the DFT melting temperatures of pure iron and iron alloyed with sulfur, silicon, and oxygen, as detailed in the previous section. The values for the electrical and thermal conductivities are in the range 1.1–$1.3 \times 10^6 \Omega^{-1}\,\mathrm{m}^{-1}$ and 100–$160\,\mathrm{W\,m}^{-1}\,\mathrm{K}^{-1}$, respectively, with the low/high values corresponding to CMB/ICB pressure–temperature conditions.

The Lorenz parameter is roughly constant on all three adiabats, indicating that the Wiedemann–Franz law is valid throughout the core. For pure iron, the Lorenz parameter varies between 2.47×10^{-8} and $2.51 \times 10^{-8}\,\mathrm{W\Omega\,K}^{-2}$, only slightly higher than its ideal value of $2.44 \times 10^{-8}\,\mathrm{W\Omega\,K}^{-2}$, while for the mixtures, it is reduced in the range 2.17–$2.24 \times 10^{-8}\,\mathrm{W\Omega\,K}^{-2}$. These values are in broad agreement with those recently reported by de Koker et al. (2012).

The calculated electrical conductivities are in good agreement with the experimental data for FeSi up to 140 GPa of Matassov (1977) and for $Fe_{0.94}$ O up to 155 GPa of Knittle et al. (1986), who reported values in the range 1.0–$1.2 \times 10^6\,\Omega^{-2}\,\mathrm{m}^{-1}$. The thermal conductivities are in agreement with recent experimental findings of Hirose et al. (2011) who reported values for the top of the outer core in the range 90–$130\,\mathrm{W\,m}^{-1}\,\mathrm{K}^{-1}$.

These estimates of thermal and electrical conductivity are two to three times higher than those previously used in the geophysical literature (e.g., Nimmo, 2007; Stacey, 2007).
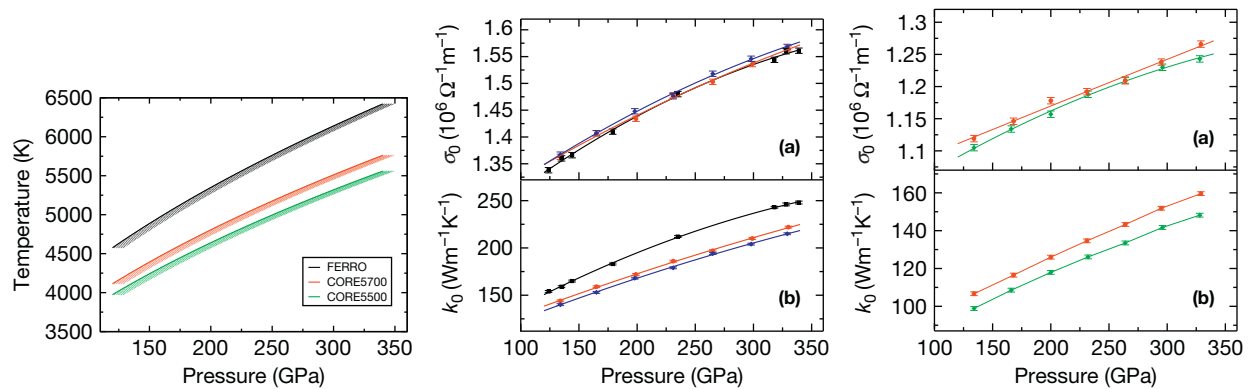
Figure 14 (left) Adiabatic temperature profiles as function of pressure anchored by three possible ICB temperatures T_{ICB}. Black curve (FERRO) corresponds to $T_{ICB} = 6350$ K, red curve (CORE5700) to $T_{ICB} = 5700$ K, and green curve to $T_{ICB} = 5500$ K. Low-pressure edges of the bands (solid line) correspond to the raw DFT–PW91 pressures and high-pressure edges to pressure corrected by 10 GPa, which is the typical DFT–PW91 underestimate of the pressure for iron at core conditions. (center) Electrical (a) and thermal (b) conductivity of liquid iron at the Earth's core conditions, computed on the FERRO (black), CORE5700 (red), and CORE5500 (blue) adiabats. Lines are quadratic fits to the first-principle raw data (symbols). Error bars (2 SD) are estimated from the scattering of the data obtained from 40 statistical independent configurations. (right) Electrical (a) and thermal (b) conductivities of liquid $Fe_{0.82}Si_{0.10}O_{0.08}$ (red) and liquid $Fe_{0.79}Si_{0.08}O_{0.13}$ (green) mixtures on the CORE5700 and CORE5500 adiabats, respectively. Error bars (2 SD) are estimated from the scattering of the data obtained from 40 statistical independent configurations. Results are obtained with cells including 157 atoms and the single **k**-point (1/4, 1/4, and 1/4), which are sufficient to obtain convergence within <1%. Reproduced from Pozzo M, Davies C, Gubbins D, and Alfè D (2013) *Physical Review B* 87: 014110.

The high thermal conductivity in particular has significant implications for the evolution of the core and the dynamo process generating the Earth's magnetic field. The convective motions in the outer core that are responsible for the Earth's dynamo are driven by a combination of thermal and chemical buoyancy sources. The strength of thermal driving is measured by the amount of excess heat that cannot be conducted down the adiabatic gradient; higher thermal conductivity increases adiabatic conduction and therefore decreases the effectiveness of thermal buoyancy relative to chemical buoyancy. Maintaining the same magnetic field with less available thermal buoyancy requires a faster core cooling rate or a higher concentration of radiogenic elements in the core or a combination of the two. Moreover, a faster cooling rate implies that the inner core, which is already thought to be a relatively young feature of the Earth (age ~1Ga; Labrosse et al., 2001), is even younger.

2.15.4   Conclusions

I have described here some ab initio techniques, based on the fundamental laws of quantum mechanics, that are currently being used to study the properties of high-pressure and high-temperature minerals. I have focused our discussion to the formulation of quantum mechanics known as DFT, with various approximations for the XC functional, and I have shown that this technique can predict very reliably a number of static and elastic properties, like low-temperature equation of states, phase transition, and elastic constants. DFT has also been successfully used to predict the vibrational properties of a large number of materials, and the examples provided here show that these predictions are in good agreement with the experimental data, at both zero pressure and high pressure. To study the high-temperature properties of solids and liquids, ab initio techniques

coupled with MD have been proven to be a powerful and reliable tool for both solids and liquids. I have illustrated this mentioning the calculation of the high-temperature elastic constants of the mantle-forming minerals $MgSiO_3$ in both the perovskite and the recently discovered postperovskite phases and the elastic behavior of hcp iron under the conditions of the Earth's inner core and the dynamic properties of liquids like diffusion and viscosity.

A major contribution to the calculation of the ab initio high-pressure and high-temperature properties of minerals has been given by the possibility of calculating free energies, and I have described how this can be done for both liquids and solids, using the technique of thermodynamic integration. The access to the free energies of materials has allowed the calculation of a number of thermodynamic properties. Here, I have described the calculation of melting properties and in particular the melting curve of iron under Earth's core conditions. I have also shown how ab initio techniques coupled with thermodynamic integration can be used to calculate chemical potentials in binary solutions and illustrated the method by showing the calculation of the chemical potentials of oxygen, sulfur, and silicon in solid and liquid iron at the Earth's core conditions. These calculations were used in conjunction with seismological data to estimate the probable composition of the Earth's inner and outer core. I have also shown that it has become possible to compute transport properties like the electrical and thermal conductivities, and I have mentioned recent calculations applied to the Earth's core.

In our description of melting properties, I have pointed out that current XC functionals do not always provide perfect agreement with the experiments. I have shown how the application of empirical corrections can improve these results, but this is not a completely satisfactory solution, as it introduces some arbitrariness in the calculations, which do not conform to our original definition of ab initio anymore. Therefore, it is

important to be able to go beyond DFT, and for this, I have mentioned QMC techniques, which I believe are sufficiently accurate and general that they will become a major player in the field of first-principles calculations of material properties. The development of these techniques will be helped by the availability of ever more powerful computers.

I have also mentioned the technique of the coexistence of phases to calculate melting curves. This technique is intrinsically very expensive, as it needs calculations performed on systems containing hundreds or even thousands of atoms. However, recently, it has just become possible to apply this technique in the context of ab initio calculations, with simulations reported on up to 1728 atom cells. I have illustrated this method with the recent calculation of the melting curve of MgO under the Earth's mantle conditions. The availability of faster computers will help make this coexistence calculations more routinely applied and possibly will also allow simulation of the eutectic behavior of solutions, in which a liquid is in coexistence with more than one solid phase.

Acknowledgments

References

Alder BJ and Wainwright TE (1959) *Journal of Chemical Physics* 31: 459.

Alfè D (1999) *Computer Physics Communications* 118: 31.

Alfè D (2003) *Physical Review B* 68: 064423.

Alfè D (2005) *Physical Review Letters* 94: 235701.

Alfè D (2009a) *Computer Physics Communications* 180: 2622, Program available at http://chianti.geol.ucl.ac.uk/~dario.

Alfè D (2009b) *Physical Review B* 79: 060101(R).

Alfè D, Alfredsson M, Brodholt J, Gillan MJ, Towler MD, and Needs RJ (2005) *Physical Review B* 72: 014114.

Alfè D and Gillan MJ (1998a) *Physical Review B* 58: 8248.

Alfè D and Gillan MJ (1998b) *Physical Review Letters* 81: 5161–5164.

Alfè D and Gillan MJ (2003) *Physical Review B* 68: 205212.

Alfè D and Gillan MJ (2004a) *Physical Review B* 70: 161101.

Alfè D and Gillan M (2004b) *Journal of Physics: Condensed Matter* 16: L305.

Alfè D, Gillan MJ, and Price GD (2002a) *Physical Review B* 65: 165118.

Alfè D, Gillan MJ, and Price GD (2002b) *Earth and Planetary Science Letters* 195: 91.

Alfè D, Kresse G, and Gillan MJ (2000a) *Physical Review B* 61: 132.

Alfè D, Price GD, and Gillan MJ (2000b) *Geophysical Research Letters* 27: 2417.

Alfè D, Price GD, and Gillan MJ (2000c) *Nature* 405: 172.

Alfè D, Price GD, and Gillan MJ (2001) *Physical Review B* 64: 045123.

Alfè D, Price GD, and Gillan MJ (2002c) *Journal of Chemical Physics* 116: 6170.

Alfè D, Price GD, and Gillan MJ (2002d) *The Journal of Chemical Physics* 116: 7127–7136.

Alfè D, Vočadlo L, Price GD, and Gillan MJ (2004) *Journal of Physics. Condensed Matter* 16: S973.

Allen MP and Tildesley DJ (1987) *Computer Simulation of Liquids*. New York: Oxford Science Publications.

Andersen HC (1980) *Journal of Chemical Physics* 72: 2384.

Anzellini S, Dewaele A, Mezouar M, Loubeyre P, and Morard G (2013) *Science* 340: 464, See also Y. Fei, Science 340, 442 (2013).

Arias TA, Payne MC, and Joannopoulos JD (1992) *Physical Review B* 45: 1538, *Physical Review Letters* 69 (1992) 1077.

Bachelet GB, Hamann DR, and Schlüter M (1982) *Physical Review B* 26: 4199.

Baroni S, de Gironcoli S, Dal Corso A, and Gianozzi P (2001) *Reviews of Modern Physics* 73: 515.

Baroni S, Gianozzi P, and Testa A (1987) *Physical Review Letters* 58: 1861.

Becke AD (1993) *Journal of Chemical Physics* 98: 5648.

Belonoshko AB, Ahuja R, and Johansson B (2000) *Physical Review Letters* 84: 3638.

Binnie SJ, Nolan SJ, Drummond ND, et al. (2010) *Physical Review B* 82: 165431.

Blöchl PE (1994) *Physical Review B* 50: 17953.

Boehler R (1993) *Nature* 363: 534.

Bonev SA, Schwegler F, Ogitsu T, and Galli G (2004) *Nature* 431: 669.

Bowler DR, Miyazaki T, and Gillan MJ (2002) *Journal of Physics. Condensed Matter* 14: 2781.

Brown JM and McQueen RG (1986) *Journal of Geophysical Research* 91: 7485.

Car R and Parrinello M (1985) *Physical Review Letters* 55: 2471.

Casula M, Filippi C, and Sorella S (2005) *Physical Review Letters* 95: 100201.

Casula M, Moroni S, Sorella S, and Filippi C (2010) *Journal of Chemical Physics* 132: 154113.

Casula M and Sorella S (2003) *Journal of Chemical Physics* 119: 6500.

Ceperley D and Alder B (1980) *Physical Review Letters* 45: 566.

Chang KJ and Cohen ML (1984) *Physical Review B* 30: 4774.

Chester GV and Thellung A (1961) *Proceedings of the Physical Society of London* 77: 1005.

Cho JH and Scheffler M (1996) *Physical Review B* 53: 10685.

D'Arco PH, Sandrone G, Dovesi R, Orlando R, and Saunders VR (1993) *Physics and Chemistry of Minerals* 20: 407.

de Koker N, Steinle-Neumann G, and Vlček V (2012) *Proceedings of the National Academy of Sciences* 109: 4070.

de Wijs GA, Kresse G, and Gillan MJ (1998) *Physical Review B* 57: 8223.

Desjarlais MP, Kress JD, and Collins LA (2002) *Physical Review E* 66: 025401.

Dreizler RM and Gross EKU (1990) *Density Functional Theory*. Heidelberg: Springer-Verlag.

Drummond ND and Ackland GJ (2002) *Physical Review B* 65: 184104.

Duffy TS, Hemley RJ, and Mao H-K (1995) *Physical Review Letters* 74: 1371.

Dziewonski AM and Anderson DL (1981) *Physics of the Earth and Planetary Interiors* 25: 297.

Feynman RP (1948) *Reviews of Modern Physics* 20: 367.

Filippi C, Healy SB, Kratzer P, Pehlke E, and Scheffler M (2002) *Physical Review Letters* 89: 166102.

Foulkes WMC, Mitaš L, Needs RJ, and Rajagopal G (2001) *Reviews of Modern Physics* 73: 33.

Frenkel D and Smit B (1996) *Understanding Molecular Simulation*. San Diego: Academic Press.

Gannarelli CMS, Alfè D, and Gillan MJ (2005) *Physics of the Earth and Planetary Interiors* 152: 67.

Giannozzi P, de Gironcoli S, Pavone P, and Baroni S (1991) *Physical Review B* 43: 7231.

Gibson JB, Goland AN, Milgram M, and Vineyard MGH (1960) *Physics Review* 120: 1229.

Gillan MJ (1990) In: Catlow CRA, Parker SC, and Allen MP (eds.) *Computer Modelling of Fluids, Polymers and Solids*. *NATO ASI series C*, vol. 293, pp. 155–188. Boston: Kluwer Academic Publishers.

Gillan MJ (1997) *Contemporary Physics* 38: 115.

Gonze X and Vigneron J-P (1989) *Physical Review B* 39: 13120.

Greenwod DA (1958) *Proceedings of the Physical Society* 71: 585.

Grimme S (2011) *Computational Molecular Science* 1: 211.

Grossman JC, Mitas L, and Raghavachari K (1995) *Physical Review Letters* 75: 3870, erratum: *ibid.* 76, 1006 (1995).

Gubbins D, Alfè D, Masters G, Price D, and Gillan MJ (2004) *Geophysical Journal International* 157: 1407.

Hamann DR, Schlüter M, and Chiang C (1979) *Physical Review Letters* 43: 1494.

Hirose K, Gomi H, Ohta K, Labrosse S, and Hernlund J (2011) *Mineralogical Magazine* 75: 1027.

Hohenberg P and Kohn W (1964) *Physics Review* 136: B864.

Hoover WG (1985) *Physical Review A* 31: 1695.

Iitaka T, Hirose K, Kawamura K, and Murakami M (2004) *Nature* 430: 442.

Jackson JM, Sturhahn W, Lerche M, et al. (2013) *Earth and Planetary Science Letters* 362: 143.

Jaffe JE, Snyder JA, Lin Z, and Hess AC (2000) *Physical Review B* 62: 1660.

Jephcoat AP, Mao HK, and Bell PM (1986) *Journal of Geophysical Research* 91: 4677.

Karki BB, Stixrude L, Clark SJ, et al. (1997) *American Mineralogist* 82: 51.

Karki BB, Wentzcovitch RM, de Gironcoli S, and Baroni S (2000) *Physical Review B* 61: 8793.

Kerker GP (1980) *Journal of Physics C* 13: L189.

Kittel C (1996) *Introduction to Solid State Physics*, 7th edn. New York: John Wiley and Sons.

Klimeš J, Bowler DR, and Michaelides A (2011) *Physical Review B* 83: 195131.

Knittle E, Jeanloz R, Mitchell AC, and Nellis WJ (1986) *Solid State Communications* 59: 513.
Kobayashi H, Kamimura T, Alfè D, Sturhahan W, Zhao J, and Alp EE (2004) *Physical Review Letters* 93: 195503.
Kohn W and Sham L (1965) *Physics Review* 140: A1133.
Körling M and Häglund J (1992) *Physical Review B* 45: 13293.
Kresse G and Furthmuller J (1996) *Computational Materials Science* 6: 15; *Physical Review B* 54 (1996) 11169.
Kresse G, Furthmüller J, and Hafner J (1995) *Europhysics Letters* 32: 729.
Kresse G and Joubert D (1999) *Physical Review B* 59: 1758.
Kubo R (1957) *Journal of the Physical Society of Japan* 12: 570.
Labrosse S, Poirier J-P, and Le Moeul J-L (2001) *Earth and Planetary Science Letters* 190: 111.
Laio A, Bernard S, Chiarotti GL, Scandolo S, and Tosatti E (2000) *Science* 287: 1027.
Lee K, Murray ED, Kong LZ, Lundqvist BI, and Langreth DC (2010) *Physical Review B* 82: 081101.
Leung TC, Chan CT, and Harmon BN (1991) *Physical Review B* 44: 2923.
Leung W-K, Needs RJ, Rajagopal G, Itoh S, and Ihara S (1999) *Physical Review Letters* 83: 2351.
Ma Y, Somayazulu M, Shen G, Mao HK, Shu J, and Hemley RJ (2004) *Physics of the Earth and Planetary Interiors* 143–144: 455.
Mandl F (1997) *Statistical Physics*, 2nd edn. New York: John Wiley & Sons.
Manten S and Lüchow A (2003) *Journal of Chemical Physics* 119: 1307.
Mao HK, Xu J, Struzhkin VV, et al. (2001) *Science* 292: 914.
Martin RM (2004) *Electronic Structure*. Cambridge: Cambridge University Press.
Masters TG and Gubbins D (2003) *Physics of the Earth and Planetary Interiors* 140: 159.
Masters TG and Shearer PM (1990) *Journal of Geophysical Research* 95: 21691.
Matassov G (1977) *The Electrical Conductivity of Iron-Silicon Alloys at High Pressure and the Earth's Core*. PhD thesis, University of California.
Mazevet S, Torrent M, Recoules V, and Jollet F (2010) *High Energy Density Physics* 6: 84.
McWilliams RS, Spaulding DK, Eggert JH, et al. (2012) *Science* 338: 1330.
Mead CA (1992) *Reviews of Modern Physics* 64: 51.
Mehl MJ, Cohen RE, and Krakauer H (1988) *Journal of Geophysical Research* 93: 8009.
Mermin ND (1965) *Physics Review* 137: A1441.
Murakami M, Hirose K, Kawamura K, Sata N, and Ohishi Y (2004) *Science* 304: 855.
Nguyen JH and Holmes NC (2004) *Nature* 427: 339.
Nimmo F (2007) *Treatise on Geophysics* 8: 217.
Nosé S (1984) *Molecular Physics* 52: 255; *The Journal of Chemical Physics*, 81, 511 (1984).
Oganov AR, Brodholt JP, and Price GD (2001) *Nature* 411: 934.
Oganov AR and Dorokupets PI (2003) *Physical Review B* 67: 224110.
Oganov AR, Gillan MJ, and Price GD (2003) *The Journal of Chemical Physics* 67: 224110.
Oganov AR, Martoňák R, Laio A, Raiteri P, and Parrinello M (2005) *Nature* 438: 1142.
Oganov AR and Ono S (2004) *Nature* 430: 445.
Ogitsu T, Schwegler F, Gygi F, and Galli G (2003) *Physical Review Letters* 91: 175502.
Parr RG and Yang W (1989) *Density-Functional Theory of Atoms and Molecules*. New York: Oxford Science Publications.
Parrinello M and Rahman A (1980) *Physical Review Letters* 45: 1196.
Perdew JP and Zunger A (1981) *Physical Review B* 23: 5040.
Poirier J-P (1991) *Introduction to the Physics of the Earth's Interior*. Cambridge, UK: Cambridge University Press.
Pozzo M and Alfè D (2008) *Physical Review B* 77: 104103.

Pozzo M, Davies C, Gubbins D, and Alfè D (2012) *Nature* 485: 355.
Pozzo M, Davies C, Gubbins D, and Alfè D (2013) *Physical Review B* 87: 014110.
Roboredo FA and Williamson AJ (2005) *Physical Review B* 71: 121105.
Santra B, Klimeš J, Alfè D, et al. (2011) *Physical Review Letters* 107: 185701.
Savrasov PY and Kotliar G (2003) *Physical Review Letters* 90: 056401.
Seto M, Yoda Y, Kikuta S, Zhang XW, and Ando M (1995) *Physical Review Letters* 74: 3828.
Shen G, Mao H, Hemley RJ, Duffy TS, and Rivers ML (1998) *Geophysical Research Letters* 25: 373.
Singh DJ, Pickett WE, and Krakauer H (1991) *Physical Review B* 43: 11638.
Sola E and Alfè D (2009) *Physical Review Letters* 103: 078501.
Soler JM, Artacho E, Gale JD, et al. (2002) *Journal of Physics. Condensed Matter* 14: 2745.
Stacey F (2007) *Encyclopedia of Geomagnetism and Paleomagnetism*, p. 91. The Netherlands: Springer.
Staroverov VN, Scuseria GE, Tao J, and Perdew J (2004) *Physical Review B* 69: 075102.
Stillinger FH and Weber TA (1985) *Physical Review B* 31: 5262.
Stixrude L and Cohen RE (1993) *Nature* 364: 613.
Stixrude L and Cohen RE (1995) *Science* 267: 1972.
Sturhahn W, Toellner TS, Alp EE, et al. (1995) *Physical Review Letters* 74: 3832.
Sugino O and Car R (1995) *Physical Review Letters* 74: 1823.
Tao J, Perdew JP, Staroverov VN, and Scuseria GE (2003) *Physical Review Letters* 91: 146401.
Tkatchenko A, Alfè D, and Kim KS (2012) *Journal of Chemical Theory and Computation* 8: 4317.
Tkatchenko A, Romaner L, Hoffmann OT, Zojer E, Ambrosch-Draxl C, and Sheffler M (2010) *MRS Bulletin* 35: 435.
Towler MD, Gillan MJ, and Alfè D (2011) Psi-k Highlight of the month, Feb. 2011.
Tsuchiya T, Tsuchiya J, Umemoto K, and Wentzcovitch R (2004) *Earth and Planetary Science Letters* 224: 241.
Umrigar CJ, Nightingale MP, and Runge KJ (1993) *Journal of Chemical Physics* 99: 2865.
Vanderbilt D (1990) *Physical Review B* 41: 7892.
Verlet L (1967) *Physics Review* 159: 98.
Vočadlo L and Alfè D (2002) *Physical Review B* 65: 214105.
Wallace DC (1998) *Thermodynamics of Crystals*. New York: Dover Publications.
Wang Y and Perdew J (1991) *Physical Review B* 44: 13298.
Wang W, Scandolo S, and Car R, unpublished.
Wannier GH (1966) *Statistical Physics*. New York: Dover Publications.
Watanabe M and Reinhardt WP (1990) *Physical Review Letters* 65: 3301.
Wentzcovitch RM, Martins JL, and Price GD (1993) *Physical Review Letters* 70: 3947.
Wiedemann D and Franz R (1853) *Annalen der Physik* 89: 497.
Williams Q, Jeanloz R, Bass JD, Svendesen B, and Ahrens TJ (1987) *Science* 286: 181.
Williamson AJ, Hood RQ, and Grossman JC (2001) *Physical Review Letters* 87: 246406.
Wookey J, Stackhouse S, Kendall JM, Brodholt J, and Price GD (2005) *Nature* 438: 1004.
Yoo CS, Holmes NC, Ross M, Webb DJ, and Pike C (1993) *Physical Review Letters* 70: 3931.
Zerr A and Boehler R (1994) *Nature* 371: 506.
Zhu J, Wang XW, and Louie SG (1992) *Physical Review B* 45: 8887.